Research Paper

# Model based mapping of a novel prototype spark ignition opposed-piston engine

S.F. Furze *, S. Barraclough, D. Liu, S. Melendi-Espina

*School of Engineering, University of East Anglia, Norwich Research Park, NR4 7TJ Norwich, United Kingdom*

## ARTICLE INFO

## ABSTRACT

Blower-scavenged opposed-piston two-stroke engines possess inherent thermodynamic advantages over four stroke engines. Increasingly well demonstrated in compression ignition form, they are less so in spark ignition form, where there is clearly room for further investigation. Using CONVERGE® CFD, in this work therefore the fuelling requirements of a novel and under-construction small-displacement, two-stroke, spark-ignition, blower-scavenged opposed-piston engine prototype were estimated using three-dimensional computational fluid dynamics simulations. Trapped air mass values generated from motored simulations were used to populate a fuel-agnostic table of speed/scavenge pressure conditions, which will significantly aid the configuration of the engine ECU. This table was tested using targeted fuelled simulations, based on bulk in-cylinder equivalence ratio. Results indicate it was able to predict the required fuel within $\pm 2$ % at 1500 rpm, 120/150/180 kPa and 3000 rpm, 150/180 kPa, within $\pm 10$ % at 3000 rpm, 120 kPa and 5000 rpm, 180 kPa, and within $\pm 20$ % at 5000 rpm, 150 kPa. It performed less well at 5000 rpm, 120 kPa where it overestimated the required fuel by over 43 %, although this was to be expected given the reduced scavenging performance at high speed, low scavenge pressure conditions. The swirl-imparting geometry also appeared to aid in flame front propagation.

## 1. Introduction

In 2021, fossil fuels provided more than 82 % of global primary energy consumption [1,2]. Reducing GHG emissions is a particularly prominent issue in the present time, though it is clearly one that faces many very significant hurdles. Indeed, in a particularly critical review, Kalghatgi raises serious questions as to whether it is even feasible to achieve 'Net Zero' decarbonisation targets in the timeframes and to the extents often stated [1]. Moreover, reducing emissions from the transportation sector is one of the most challenging, owing to its reliance on energy-dense hydrocarbon fuels, which are very difficult to replace, especially in cases such as long-haul road-freight transport [1,3]. Whilst electrification using BEVs is commonly the most discussed decarbonisation strategy, it is not often well-suited to all use-cases, such as those described above. Furthermore, there is growing concern over its

sustainability and environmental impact, not only in terms of GHG emissions, but also in terms of resource intensity, end of life material disposal, human toxicity potential and ensuring the additional electricity generation comes from low-carbon sources [1,4]. A more pragmatic assessment is that a diverse approach to decarbonisation of these sectors is far more likely to be successful in reducing emissions overall, than a prescribed 'one-size-fits-all' scenario. This includes electrification but also other strategies, like alternative fuels and improvements in internal combustion engine technology [4–6]. Such a pragmatic view is particularly pertinent given the findings of a recent study by Burton *et al.* which considered a method of determining the GHG emissions rates of different powertrains by more accurately representing the U.S. electricity grid, instead of relying on average grid emission rates. It was concluded that BEVs do not lead to uniform reductions in emissions rates in comparison to HEVs, and in many scenarios have higher emissions

---

rates [5].

Modern internal combustion engines typically demonstrate high levels of resilience to varying loads, operating environments, and fuel quality, as well as a long service life. Improvements in engine lubrication, the use of alternative engine operating cycles, and numerous other developments have all contributed to significant engine efficiency and emissions improvements [3,7,8]. Further developments have been aided in recent years by increasingly powerful computer simulation capabilities, as well as more precise levels of engine control [3,9]. For example, in their Skyactiv-X engine, Mazda employs a highly sophisticated fuel injection and engine control strategy that enables the use of 'spark-controlled compression ignition' or 'SpCCI'. Utilising higher compression ratios and extremely lean combustion in such operation, the engine retains the controllability of using a spark plug to ignite a flame front, whilst significantly increasing efficiency by using the resulting increase in temperature and pressure ahead of the flame to initiate autoignition of the remaining fuel charge. Toyota's 2.5 L SI architecture is another notable example: This engine exhibits a peak BTE of around 40 % (depending on powertrain configuration) yet is SI exclusively [3].

Many modern, heavy-duty CI engines exhibit higher peak thermal efficiencies than SI engines – this is to be expected given the higher compression ratios utilised and their more advantageous cylinder volume to surface-area ratios [3,4]. Like their SI counterparts, these have been improving: One recent production diesel engine by Weichei demonstrated in excess of 50 % peak BTE; this engine is designed for road haulage applications [9]. Westport Fuel Systems further achieved 51.5 % peak BTE in a hydrogen-diesel dual fuel engine using their proprietary HPDI® injection system, built on a 50 % peak BTE Scania diesel engine. The dual fuel engine can also run solely on diesel fuel if required [10].

In conjunction with improvements in engine efficiency, alternative (i.e., non-fossil-fuel based) fuels are another significant area of research in both CI and SI engines alike. Though in some cases, concerns exist in relation to sustainable and scalable supply, many such fuels have been found suitable for internal combustion engines through extensive research [3,4,6,7,9,11]. Noting the sub-optimal combustion characteristics of ammonia, a particularly impressive work by Lhuillier *et al.* quantified an experimental database for an ammonia-hydrogen dual fuel SI engine of modern architecture. Hydrogen enrichment of between 0 % and 60 % by volume was evaluated, and it was found that low and moderate hydrogen addition achieved the best IMEP and thermal efficiency values, with slightly fuel rich and fuel lean mixtures respectively [12]. The authors extensive review of prior works further noted the feasibility of *in-situ* hydrogen production through a catalytic cracking reactor, as well as the use of SCR for exhaust after-treatment.

The fact that they have been successfully demonstrated using fuels as challenging as an ammonia-hydrogen blend, and still delivered satisfactory performance, is a testament both to the fuel-flexibility and the advanced technological state of modern internal combustion engines. However, the vast majority of modern internal combustion engines – including all of the above examples – use a four-cycle architecture [7,8]. Though four-cycle engines are very well proven, the opposed-piston two-stroke (or 'OP2S') engine offers fundamental thermodynamic advantages, such as a high stroke to bore ratio, decoupling of pumping work from the pistons, the lack of a cylinder head and valve train, and two-cycle operation, though this is not an exhaustive list. Not only do these advantages allow high peak BTEs, but they also contribute to consistently high efficiencies over a wide range of operating conditions [13–15].

The OP2S architecture makes use of two opposing pistons in the same cylinder, the combustion chamber being formed mostly by the two piston crowns around inner dead centre. Cylinder porting facilitates gas exchange towards outer dead centre, usually driven by an external scavenging system since the pistons do little of the pumping work. Although the scavenging pump requires power to drive it, because the pumping work is decoupled from piston motion the load is external to

the cylinder, offering a further degree of control and scope to improve efficiency [13,14]. In these 'blower scavenged' engines, lubrication is via a closed system, much like a four-cycle engine. This should not be confused with the typically total loss system found in crankcase-scavenged engines, though even piston-ported engines with separate lubrication systems have historically suffered from excessive oil consumption [16].

More recently however, Achates Power – a company based in the United States of America and formed in 2004 – has extensively redeveloped the OP2S architecture, to the extent that they have resolved many of the mechanical issues that made piston-ported architectures less popular, including the difficulties associated with gearing together the two separate crankshafts that their OP2S engines utilise [17]. They also succeeded in addressing the problem of excessive oil consumption: In a test of their A48-1 single cylinder engine, results indicated that fuel specific oil consumption (measured with a sulphur-tracing system) has been reduced to 0.04 % fuel on a weighted drive-cycle average basis, and 0.052 % at rated load [16]. It was highlighted that with increasing run-time, the oil-consumption of the test engine seemed to decrease further – it is believed this is due to the liner and ring pack 'wearing in' [16]. In achieving these results, the authors noted the importance of the liner surface, identifying shortcomings in traditional honing methods that were used, for example, in the historic Detroit® two-stroke diesel engines. Not only did this provide leakage paths for lubricating oil into the ports, but it also retained a significant quantity of oil on the liner surface. They describe the application of modern industry standard practices to their engine, such as a laser ablation method developed by Gehring that allows more precise control over liner surface design, as well as liner cooling strategies to reduce bore distortion at temperature [16]. In addition to the liner itself, they have undertaken significant analyses on other aspects of the cylinder, including the piston pins, ring packs, skirts, and crowns [16]. Test results from several of their multi-cylinder engines show very low pollutant formation as well as high thermal efficiencies across a wide range of operating conditions. One of their engine architectures recently demonstrated best in class fuel efficiency and emissions in heavy duty fleet service trials, and another engine (engineered in partnership with Cummins) has been selected as a powerplant for a US Army combat vehicle due to its high efficiency, high power output and physical compactness [18,19].

Like most historic examples, the OP2S engines of Achates Power currently are mostly compression ignition architectures, and this includes a GCI engine [17]. Interestingly though, in 2022 they helped form the 'Hydrogen Opposed Piston Engine Working Group' – a consortium of parties with an interest in hydrogen-fuelled OP2S engines, citing the increasing interest in hydrogen combustion [20,21]. Then, in 2023 and in partnership Argonne National Laboratory, Achates Power also succeeded in initial testing of a single-cylinder, purely hydrogen CI OP2S engine. The authors explored strategies of non-premixed CI as well as 'partial PCCI', though they noted that the compression ignition of solely hydrogen fuel is very challenging to exploit outside of a narrow operating range, due to its resistance to autoignition [22].

It is clearly well-demonstrated that the OP2S architecture possesses thermodynamic advantages over conventional four-cycle engines, and the compression ignition of fuels such as gasoline or even hydrogen in OP2S engines is a promising and important research area. Literature on SI OP2S engines appears much less comprehensive than it is for CI OP2S engines though. Technical challenges do exist, such as the large flame propagation distance from the spark plug, which is generally confined to the cylinder edge, to the other side of the combustion chamber. Despite this, historic examples include Simpson's balanced two-stroke from the early 20th Century, a crankcase-scavenged engine that used a 'folded crank' mechanism [23], as well the later Vincent Airborne Life Raft Engine, and the experimental 'Africar' engine. The Vincent engine used a central cylinder as a scavenge pump to push a fresh charge into the two cylinders on either side of it, while the Africar engine was a carburetted, blower scavenged engine that ran, but was never tested [24].
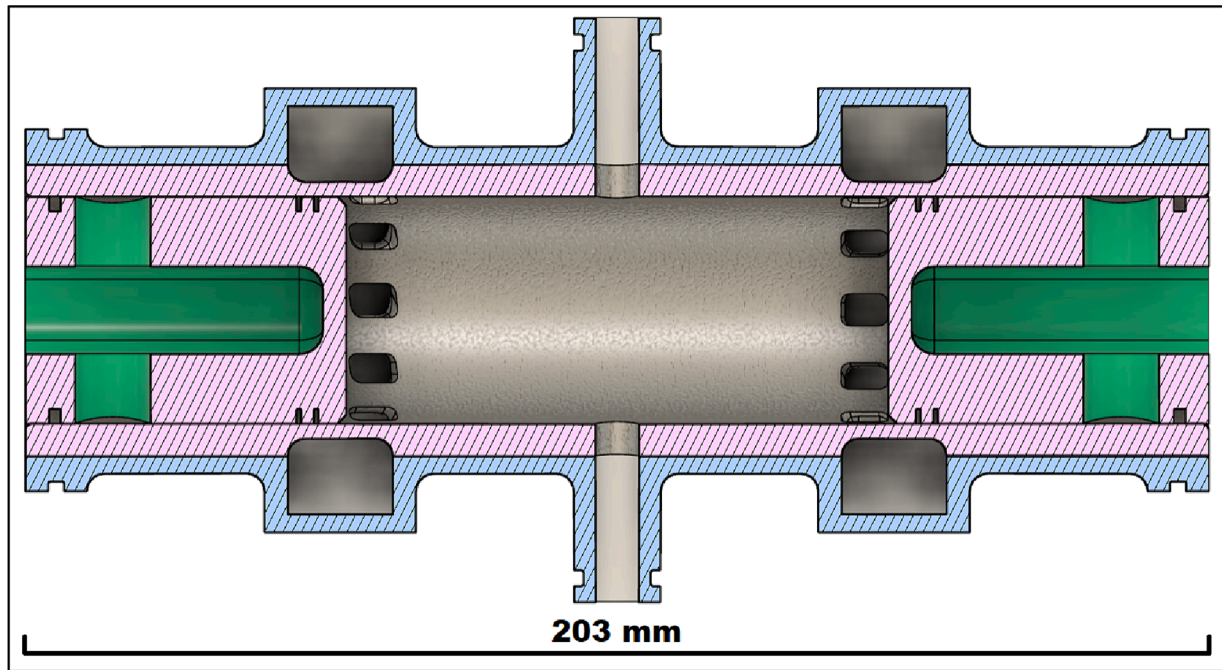
**Fig. 1.** Cross section of engine cylinder liner and block, viewed from above [39].

More recently, Ma *et al.* conducted simulations into a blower-scavenged SI OP2S architecture, including investigating the propensity of an OP2S gasoline engine to 'knock', and they have also experimentally characterised the combustion behaviour of gasoline in an OP2S engine made from two modified 125 cc engines. In this case, the engine did use a separate scavenge pump driven separately via an electric motor, where the authors used two fixed scavenging pressures of 110 kPa and 120 kPa [25,26]. More unusual architectures researched include the subject of patent no. US9303637B2, which utilises a valve-in-piston approach to connect a scavenging cylinder to the combustion cylinder [27], and other arrangements including free-piston engines, swashplate based engines and even an opposed-piston engine with a toroidal cylinder [28–30]. Nevertheless, there is clearly space for further investigation into SI OP2S engines of similar construction to their increasingly well-proven CI counterparts [13,31]. This is especially true in applications where high torque at low engine speed is not a key requirement, where there may also exist the possibility of exploiting ultra-lean combustion strategies – particularly so with hydrogen, for example [22,32].

In this work therefore, a map of the fuelling requirements of a novel, small-displacement, blower-scavenged OP2S engine prototype will be estimated using 3D computational fluid dynamics simulations, by identifying the trapped mass of air in the engine cylinder. Important engine parameters are detailed alongside the air-side surfaces of the cylinder, the pistons and intake and exhaust ports. Case-setup details, including rationale for any assumptions/estimations required and the caution with which the results should be interpreted, are described using CONVERGE® CFD, taking advantage of the port-sealing capabilities of the solver to control the flow regime to closely mimic piston-porting events [33]. The simulation results are an important aid to testing the engine prototype, since they will be used to configure the ECU. They also provide a useful discussion for the engine scavenging behaviour.

## 2. Rationale and methodology

The engine control unit requires a lookup-table to determine the amount of fuel the engine requires under different operating conditions [7]. Given the lack of empirical fuelling data for this unusual prototype, the table was generated by simulating the air-side engine geometry

using 3D CFD, to estimate the amount of air trapped within the cylinder of the engine at different engine speeds and scavenging pressures. To conduct these simulations, CONVERGE® CFD was used. CONVERGE generates the (cartesian) volume mesh at runtime, and crucially, can control flow between different regions of a flow domain based upon the proximity of user-specified surface mesh geometries, and thereby emulate piston-porting behaviour like that seen in an opposed-piston engine [33–36]. From the results generated, it is then possible to estimate the required fuel mass to achieve a desired air/fuel ratio for almost any desired fuel [7].

### 2.1. Prototype engine configuration

The prototype design consists of a single cylinder, orientated horizontally, with two crankshafts linked to a common output shaft via toothed pulleys and a timing belt. It has been designed and is currently being built at the University of East Anglia, whilst taking advantage of commercially produced parts, where possible. It is a bar-stock engine – that is the components are machined using CNC and manual machine tools from metal bar stock, rather than from specially made castings. The design builds upon earlier, tentative explorations into the feasibility of manufacturing such an item, although the new prototype bears little resemblance to the earlier air-cooled design [37]. This consisted of a finned square cylinder block that comprised the main structure of the engine, supporting two metal plates that, in turn, supported the crankshaft bearings. Some of the internal geometry of this cylinder block forms a core of the new prototype, but the design is being altered significantly and incorporated inside a much larger structure that now includes water-cooling. This will be discussed in far greater detail in future works, but the cylinder bore and stroke specifications remain the same at 39 mm bore, and 2 × 41.5 mm stroke. This was defined by the availability and cost-effectiveness of commercially produced motorcycle crankshafts, in this case for a Lexmoto TD50Q [38]. Whilst the crankshafts themselves do not preclude the configuration of a larger bore diameter, the availability of piston rings and gudgeon pins for the same motorcycle engine design provided adequate justification for retaining the original cylinder bore specification.

The trapped volume of the engine depends on the phasing between the exhaust and intake pistons, as does the maximum volume between
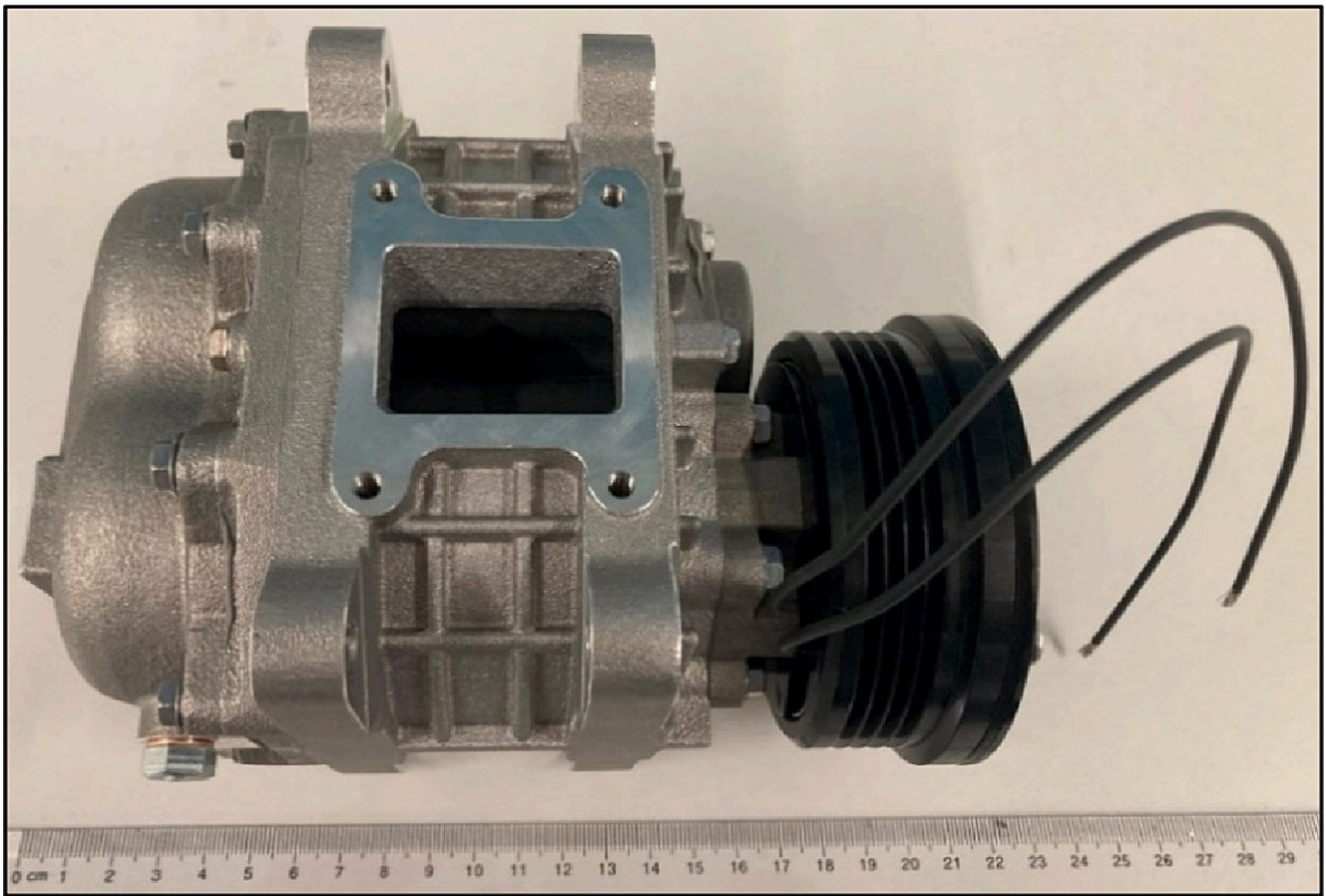
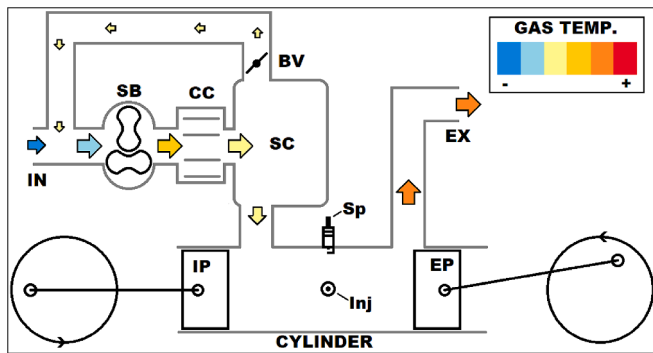**Fig. 2.** Ogura TX02 Roots Type Supercharger.



**Fig. 3.** OP2S Scavenging System: IN = Intake, SB = Scavenging Blower, CC = Charge Cooler, SC = Surge Chamber, BV = Bypass Valve, IP = Intake Piston, Sp = Spark Plug, Inj = Injector, EP = Exhaust Piston, EX = Exhaust.

the two piston crowns. With the crankshaft phase difference set at 18 CAD, the trapped volume is approximately 79 cm$^3$, and the maximum volume approximately 110 cm$^3$. The cylinder block is retained inside the main engine structure and surrounded by coolant, and a cross-section of it and the cylinder liner and pistons, as rendered in Autodesk Fusion360®, is shown in Fig. 1 [39]:

Note that in Fig. 1, the pistons are a simplified representation of the real thing and are not shown correctly in phase with each other; they are each located at ODC to make the liner ports visible. The intake ports are to the left, the exhaust ports to the right, and both have a nominal height of approximately 8 mm. The liner is made of cast iron material and the galleries that surround the ports in the cylinder liner have a square cross-

section at the outer edge, which was chosen to increase the cross-sectional area compared to rounded edges. This design was further intended to aid machinability in a manual lathe on the basis that a standard internal grooving tool could be used, see for example [40] for clarification. Also visible in Fig. 1 are the openings for two Bosch HDEV-5–1 direct injectors, located in the centre of the cylinder to inject the fuel directly; a countersink sized to fit part of the injector body is not shown [41]. Using only one injector might risk excessive fuel spray impingement on the cylinder wall due to the position of the injector on the side of the cylinder, combined with the small cylinder bore, so the provision for a second, diametrically opposed injector is included if it is found necessary. Indeed, diametrically opposed injectors are used in some CI OP2S engines – where ignition occurs as the fuel disperses into the high-temperature, high-pressure atmosphere between the two piston crowns – for better fuel distribution, see for example [42,43]. It is noted however that in this SI prototype, only one injector will be used initially due to the small engine size, which might already risk fuel flow rates that are (perhaps considerably) lower than in the original intended application of the injector.

The output shaft, which is situated at the bottom of the engine, drives the oil pump and governor via internal gearing as well as the GDI pump via a cam. A Roots-type blower will provide scavenging pressure, in this case a TX02 Supercharger by Ogura as shown in Fig. 2; this is also driven by the output shaft, via a poly-vee belt situated at the front of the engine [24,44].

The TX02 (one of the smallest Roots-blowers available) is straight-lobed, and since straight-lobed blowers produce pulsating outputs and the prototype uses a single cylinder, a large air storage volume or 'surge chamber', is being incorporated between the blower discharge, and the intake gallery [7]. The principle aims of this chamber, in conjunction
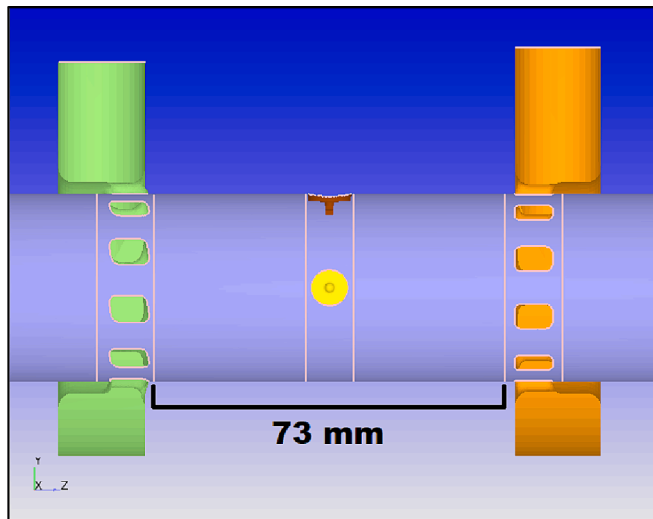
**Fig. 4.** Cross Section Showing Cylinder (purple), Intake Gallery (green) and Exhaust Gallery (orange). (For interpretation of the references to colour in this figure legend, the reader is referred to the web version of this article.)

with a bypass valve, are to reduce pressure fluctuations as well as to regulate the scavenging pressure. A simplified schematic of how the engine scavenging system is intended to work is shown in Fig. 3 [17]:

In, the coloured arrows are a simplified representation of air flow, sized according to flowrate and coloured according to temperature; both scales are for visual indication only and are not intended to be an accurate representation. Opening the bypass valve will cause pressurised air in the surge chamber to flow back to the intake of the blower, displacing incoming atmospheric air and reducing the net amount of air pumped into the engine. In so doing, the pressure in the surge chamber will drop: By controlling the pressure in the surge chamber (i.e., the scavenging pressure), the air flow through the engine can be varied. This avoids the need to throttle the intake of the blower, which could cause the pressure ratio across it to rise unacceptably. The crankshaft phasing (not shown to scale above) of the engine has been initially set to 18 degrees; that is the exhaust crankshaft leads the intake crankshaft by 18 crank angle degrees.

## 2.2. Structural geometry

The following geometry is used in all the simulation cases and closely reflects that of the air-side surfaces of the cylinder block and liner assembly detailed in Fig. 1, but with the addition of an injector tip and spark plug tip to seal the flow domain.

### 2.2.1. Intake and exhaust porting

The cylinder liner intake ports feature a swirl-inducing geometry intended to aid fuel mixing, which was achieved by way of radially offsetting the central port axis from the cylinder centreline by 10 mm. Because these ports also point slightly inwards towards the axial centre of the cylinder by 15 degrees, where they intersect the inner liner surface their shape is stretched between opposite corners. This has the effect of increasing the intake port height such that the actual phase difference (i. e., between EPO and IPO) is approximately 15 CAD, even though the crankshaft phasing is 18 CAD. Fig. 4 shows a cross section of the (airside) engine cylinder and porting geometry in CONVERGE Studio®, in which the stretched intake port shape is easier to see. Like all the surface geometry in the simulation, the surface meshes are composed of triangular elements, but the individual triangle edges have been hidden for the sake of clarity [34].

In addition to the swirl-inducing geometry of the intake liner ports, a spiral-like shape is used for the intake gallery by way of the gallery intake being offset. Fig. 5 shows the intake and exhaust galleries of the engine where this is shown [34]:

Whilst similarly pointing inwards axially, the exhaust liner ports feature a slightly larger nominal width of 5.5 mm as opposed to 5 mm for the intake ports, and the exhaust gallery outlet also extends the full width of the gallery. By increasing the available cross sectional flow area through which (and the resulting volume into which) the exhaust gases initially flow, the greater widths of both the exhaust liner ports and the gallery outlet are intended to account for the increased volume of the burned mixture leaving the cylinder over the cooler intake air entering.

### 2.2.2. Injector and spark plug

The spark plug is positioned in the axial centre of the cylinder by necessity, with the tip protruding just past the inner liner surface. It is expected that the maximum gas velocities at the time of ignition will be close to the inner surface of the liner, which may aid early flame propagation. Fig. 6 shows an isolated cross-section of the centre of the cylinder, indicating the approximate positions of the spark plug and the injector tip, which is also located in the axial centre of the cylinder [34].
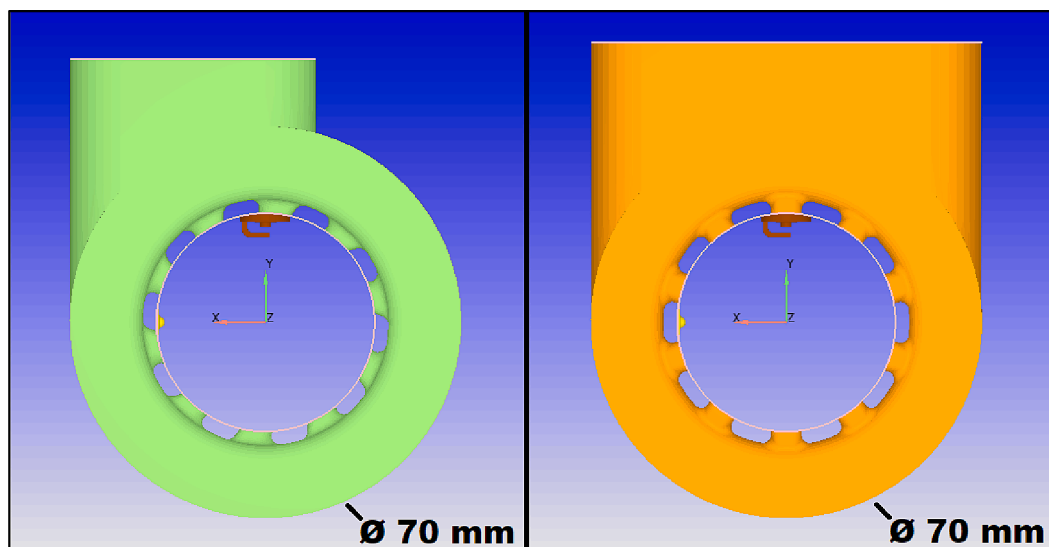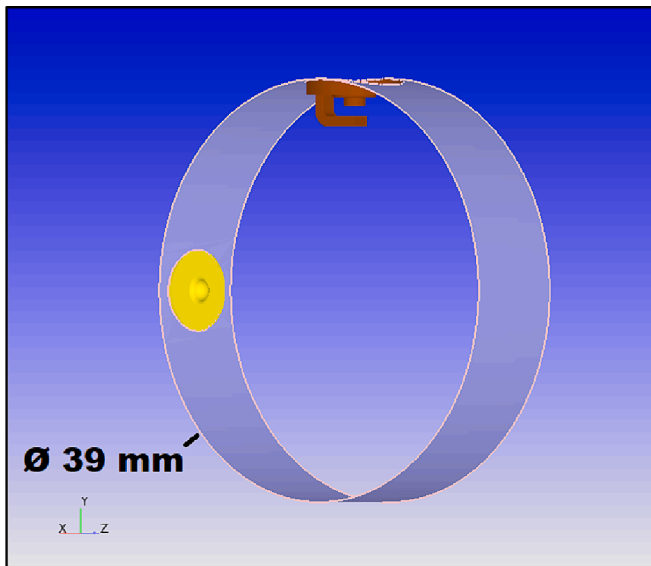


**Fig. 5.** Left: View of Intake Gallery from Cylinder End; Right: View of Exhaust Gallery from Cylinder End.

**Fig. 6.** Isolated View of Central Part of Cylinder (purple), with Injector Tip (yellow) and Spark Plug Tip (brown). (For interpretation of the references to colour in this figure legend, the reader is referred to the web version of this article.)

When viewed from the intake end of the liner, the radial position of the injector is 90 degrees anticlockwise from the spark plug. This way, a second diametrically opposed injector could be added later with less risk of spray directly impinging the spark plug electrodes. However, the second injector tip has not been included here to reflect the initial prototype testing strategy that will be employed, where only one injector will be used.

### 2.2.3. Piston crowns and cylinder

Both the intake and exhaust pistons feature flat piston crowns, but with a chamfered edge. Fig. 7 shows the complete geometry used for simulation where this is clearly visible [34].

Note that for the purposes of simulation the piston crowns and skirts are separate boundaries, but for ease of viewing are shown of the same colour. Not visible in the above are the intake, exhaust, cylinder end and piston bottom boundaries [34].

### 2.3. Boundary conditions

Configuring the simulations required some simplifications of the boundary conditions associated with the geometry above. For example, the pressure in the surge chamber will likely fluctuate over each engine cycle but attempting to model this by including the surge chamber, scavenge blower, bypass valve, and charge cooler (and associated ducting) in the simulation geometry would markedly increase the computational domain. A less computationally expensive approach was to consider the pressure in the intake gallery over one engine cycle, for a time-averaged (constant) value. Located at the top of the intake gallery in Fig. 7, the cylinder intake boundary was therefore defined as the meeting point of the surge chamber and intake port gallery, to reduce the computational domain. The pressure boundary condition was configured as a series of fixed scavenging pressures from 110 kPa to 180 kPa in 10 kPa increments, and by similarly defining the engine speeds as a series of 8 values from 1500 rpm to 5000 rpm in 500 rpm increments, an $8 \times 8$ array of values was generated. The simulation results of this array can then be used to estimate the required fuel for each condition using Eq. (1):

$$m_f = m_a * \frac{1}{\lambda}, \tag{1}$$

where $m_f$ is the mass of fuel, $m_a$ is the trapped air mass, and $\lambda$ is the air/fuel ratio [7].

A similar simplification was required for the intake temperature boundary condition because the blower discharge will be at a higher temperature than ambient [7]. The charge cooler will remove some of this heat, though the bypass valve complicates matters by displacing some of the incoming (cooler) atmospheric air at the blower intake. However, the surge chamber is over 700 cc in volume – significantly larger than the swept volume of the engine – so intake air may reside
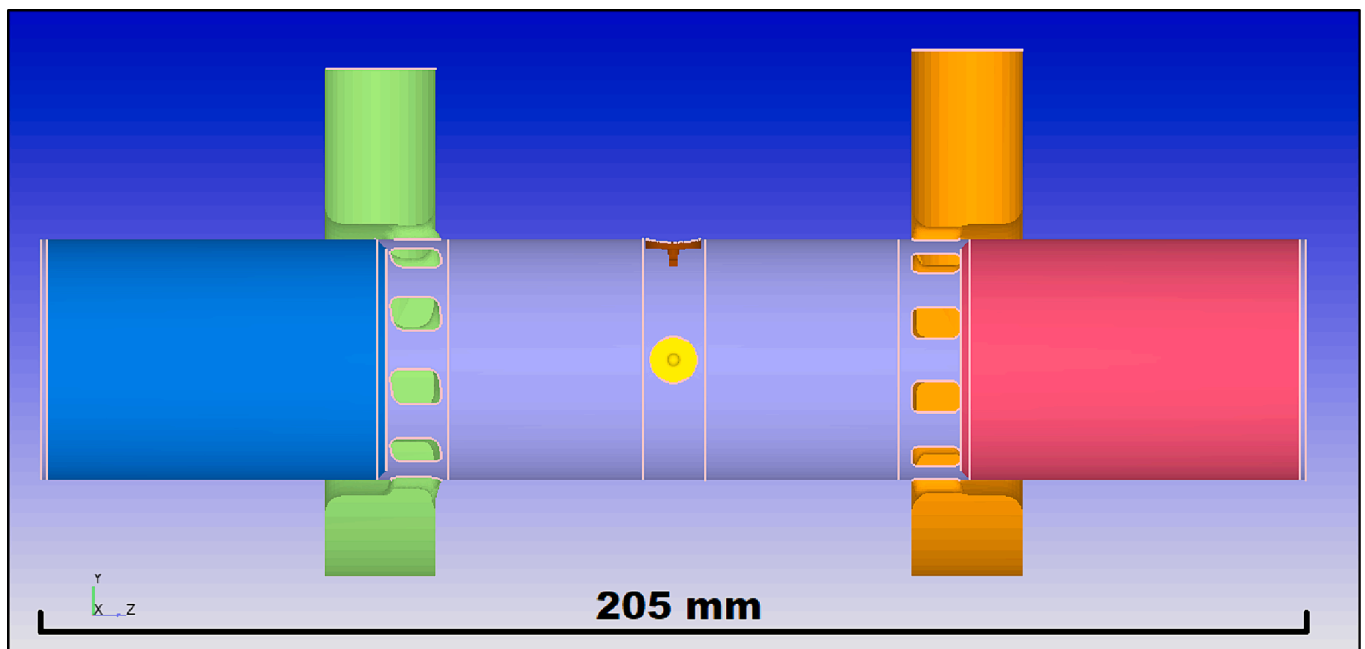


**Fig. 7.** Simulation Geometry; Cylinder (Purple, cutaway), Intake Gallery (Green, cutaway), Exhaust Gallery (Orange, cutaway), Intake Piston (Blue), Exhaust Piston (Pink), Injector Tip (Yellow) and Spark Plug Tip (Brown). (For interpretation of the references to colour in this figure legend, the reader is referred to the web version of this article.)

**Table 1**

Geometry Boundary Conditions. Note that 'Direction' represents the normal direction of the piston crowns, and 'Phase' the difference between crankshaft position.

| Name | Type | Movement | Θ (Direction) | Φ (Phase) | Temperature |
|------|------|----------|---------------|-----------|-------------|
| Cylinder | Wall | Fixed | N/A | N/A | 400 K |
| IntakeCrown | Wall | Translating | 0° | 0° | 400 K |
| IntakeSkirt | Wall | Translating | 0° | 0° | 400 K |
| IntakeBottom | Wall | Translating | 0° | 0° | 400 K |
| ExhaustCrown | Wall | Translating | 180° | −18° | 450 K |
| ExhaustSkirt | Wall | Translating | 180° | −18° | 450 K |
| ExhaustBottom | Wall | Translating | 180° | −18° | 450 K |
| INPortRing | Wall | Fixed | N/A | N/A | 350 K |
| EXPortRing | Wall | Fixed | N/A | N/A | 450 K |
| Sparkplug | Wall | Fixed | N/A | N/A | 550 K |
| Inj1 | Wall | Fixed | N/A | N/A | 400 K |
| CylinderEnds | Wall | Fixed | N/A | N/A | 400 K |

**Table 2**

Initial Conditions for Regions at −272 CAD.

| Region | Pressure | Temperature | Species Mass Percentage |
|--------|----------|-------------|-------------------------|
| Cylinder Volume | 600,000 Pa | 1200 K | $N_2$ 76 %, $O_2$ 11.3 %, $H_2O$ 12.7 % |
| Intake | Case Specified | 350 K | $N_2$ 76.7 %, $O_2$ 23.3 % |
| Exhaust | 101,325 Pa | 800 K | $N_2$ 76 %, $O_2$ 11.3 %, $H_2O$ 12.7 % |

there for several engine cycles before it reaches the intake gallery and be warmed by the surge chamber surfaces. Since these surfaces are part of the main engine structure the air temperature was set at a value of 350 K (approximately 78 °C). This is a known thermostat opening temperature and was chosen because the prototype is water-cooled, on the basis that the main engine structure will approach coolant temperature [45]. For the intake species, air is represented as 23.3 % oxygen and 76.7 % nitrogen (CONVERGE recommended values). As there are no combustion events, exhaust backflow is of much less interest in these motored simulations, so the species were rounded to the nearest whole percent at 23 % oxygen and 77 % nitrogen. The exhaust outlet temperature and pressure boundary conditions have been set at 800 K and 101,325 Pa respectively; these were estimated with guidance from CONVERGE example case literature, as were the other surface boundary conditions listed in Table 1 [33,34].

All of the above estimations, including those guided by CONVERGE and other literature, are made because there are no empirical test data for the engine; recall that the simulations were performed to guide the configuration of the engine ECU, such that empirical data can be gathered. Indeed, on the prototype engine there is provision for air temperature sensors for the blower discharge, the main surge chamber, and the exhaust, as well as a MAP sensor attached to the surge chamber. Once the engine has run, data from these sensors could naturally be used to configure more accurate simulations.

### 2.4. Flow-control, initial conditions, and simulation duration

Because CONVERGE can closely mimic the port-sealing events in piston-ported engines, the flow domain was split into three distinct regions: Intake, Cylinder and Exhaust. By correctly configuring the seal geometry (i.e., around the cylinder ports and piston crowns), as the pistons move, the solver controls flow between these regions based on the proximity of the cylinder crowns to the ports. At the start of the simulation at −272 CAD, the intake and exhaust ports are closed and there is no connection between the three regions. At this time, both pistons are moving outwards and EPO is imminent; −180 CAD represents outer dead centre for the intake piston during the first engine cycle. The initial species, pressure, and temperature conditions in all three regions are summarised in Table 2 [34–36,46].

The species in both the cylinder and exhaust regions reflect a burned

mixture for hydrogen/air, based upon data from the CONVERGE example case library [34]. By beginning the simulation shortly before EPO and artificially increasing the in-cylinder pressure and temperature, the result is an initial exhaust blowdown at EPO. The purpose of the blowdown was to rapidly establish an in-cylinder motion of gases from an initially stationary in-cylinder flow-field, because in the real engine there will likely be significant in-cylinder motion of the burned mixture before EPO. However, this approach may introduce large velocity gradients at first, so after the initial blowdown each case was run for a total of three complete engine cycles until 900 CAD. This allowed time for any resulting mathematical instabilities (and any other errors), to gradually disperse, whilst balancing the similarly important consideration of not exceeding the available computational memory; [46]. The simple burned mixture also provides a useful method of monitoring the scavenging performance by reviewing the $H_2O$ mass concentration in the cylinder between cycles. Although this burned mixture is based on models for hydrogen combustion, $H_2O$, $O_2$ and $N_2$ are common species to many combustion reactions. Additionally, the precise mixture composition was of less interest than the change in $H_2O$ mass concentration per cycle [34]. Data files for material properties were sourced from the CONVERGE example case library; these are based upon an enhancement on a skeletal kinetic model by Liu *et al.* for primary reference fuel oxidation [34,47].

### 2.5. RANS equations

CFD simulations are built upon the conservation of mass, momentum, and energy [48]; for a general introduction, see [49] and [50]. Using CONVERGE, in this work a RANS method was implemented [33]. In compressible form, the RANS equations, which govern the conservation of both mass and momentum are given by [35]:

$$\frac{\partial \overline{\rho}}{\partial t} + \frac{\partial \overline{\rho}\widetilde{u_j}}{\partial x_j} = 0, \tag{2}$$

and

$$\frac{\partial \overline{\rho}\widetilde{u_i}}{\partial t} + \frac{\partial \overline{\rho}\widetilde{u_i}\widetilde{u_j}}{\partial x_j} = -\frac{\partial \overline{P}}{\partial x_i} + \frac{\partial}{\partial x_j}\left[\mu\left(\frac{\partial \widetilde{u_i}}{\partial x_j} + \frac{\partial \widetilde{u_j}}{\partial x_i}\right) - \frac{2}{3}\mu\frac{\partial \widetilde{u_k}}{\partial x_k}\delta_{ij}\right] + \frac{\partial}{\partial x_j}\left(-\widetilde{\rho u_i' u_j'}\right), \tag{3}$$

where ρ is density, u is fluid velocity, P is pressure, μ is dynamic viscosity, and $\delta_{ij}$ is the Kronecker delta. Here, tilde is used to denote properties that have been Favre averaged, which in the case of fluid velocity is defined as [35]:

$$\widetilde{u_i} \equiv \frac{\overline{\rho u_i}}{\overline{\rho}}, \tag{4}$$

where the overbar represents Reynolds averaged values. Favre averaging is a density-weighted average and is useful in situations where there are variations in density, such as an internal combustion engine in
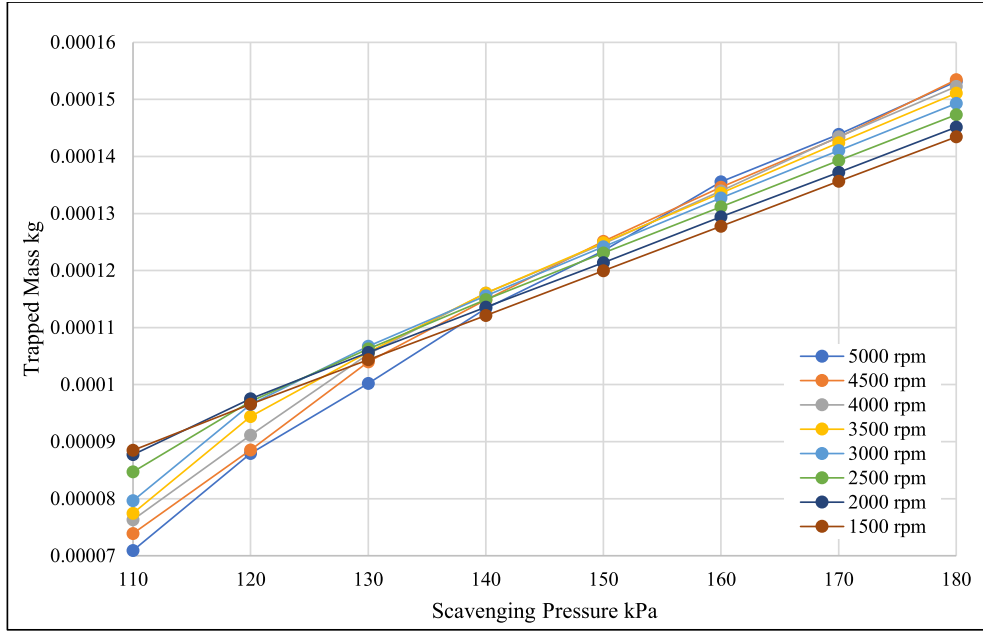
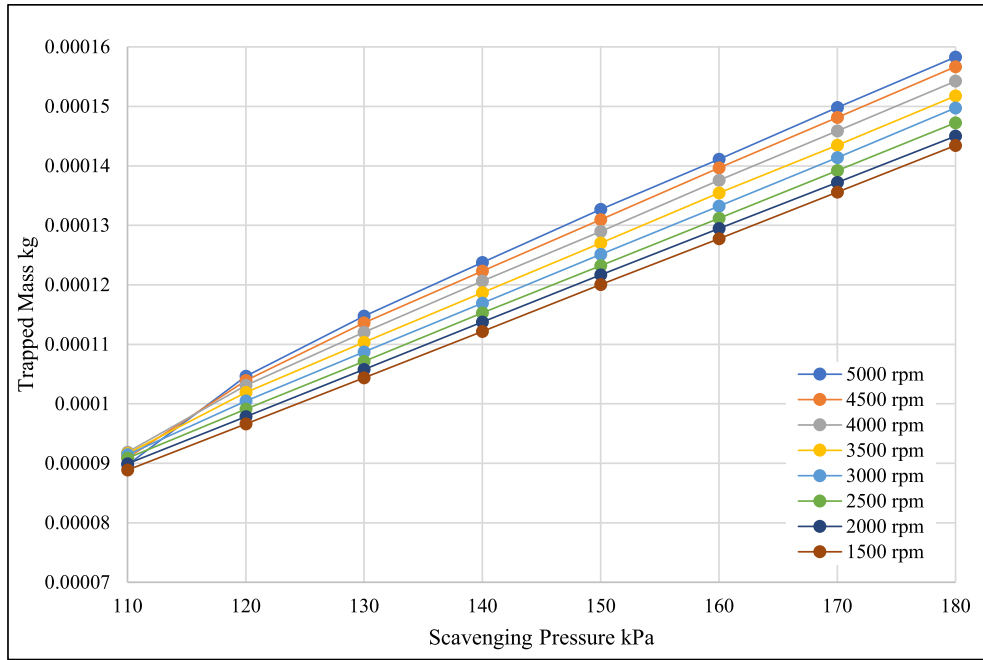**Fig. 8.** In Cylinder Trapped Mass of all Species, 1st Engine Cycle.



**Fig. 9.** In Cylinder Trapped Mass of all Species, 2nd Engine Cycle.

which there is compression and expansion of the cylinder volume [7,51]. The argument of the rightmost term in Eq. (3) represents the effect of turbulence, and involves Reynolds stresses [35]:

$$\tau_{ij} = -\overline{\rho \widetilde{u_i' u_j'}}. \tag{5}$$

To model the Reynolds stresses, a k-ε turbulence model was chosen. Like other RANS methods, this models the Reynolds stresses by assuming that the mixing caused by turbulence introduces an effective viscosity $\mu_t$, that acts in addition to the dynamic viscosity, defined as [7,35]:

$$\mu_t = C_\mu \rho \frac{k^2}{\varepsilon}, \tag{6}$$

where $C_\mu$ is a model constant, k is turbulent kinetic energy, and ε is the rate of dissipation of turbulent kinetic energy [7,35]. In these simulations, the Rapid Distortion RNG k-ε turbulence model proposed by Han and Reitz was implemented [52]. In this model, the Reynolds stress tensor is written as [35]:

$$\tau_{ij} = -\overline{\rho \widetilde{u_i' u_j'}} = 2\mu_t S_{ij} - \frac{2}{3} \delta_{ij} \left( \rho k + \mu_t \frac{\partial \widetilde{u_i}}{\partial x_i} \right), \tag{7}$$

where $S_{ij}$ is the mean strain rate tensor [35]:

$$S_{ij} = \frac{1}{2} \left( \frac{\partial \widetilde{u_i}}{\partial x_j} + \frac{\partial \widetilde{u_j}}{\partial x_i} \right), \tag{8}$$
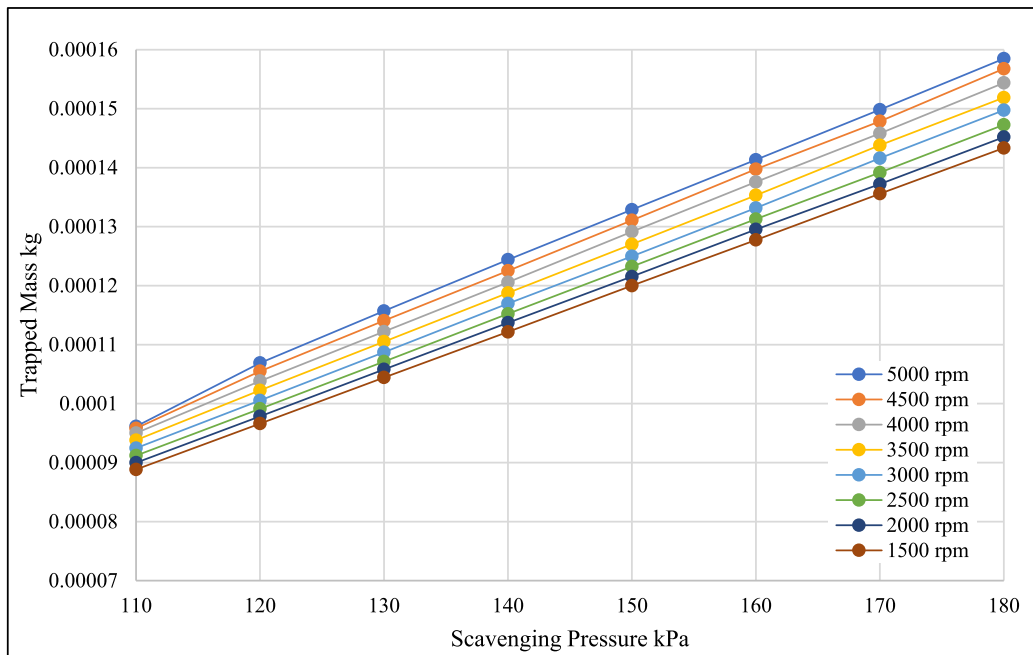
**Fig. 10.** In Cylinder Trapped Mass of all Species, 3rd Engine Cycle.



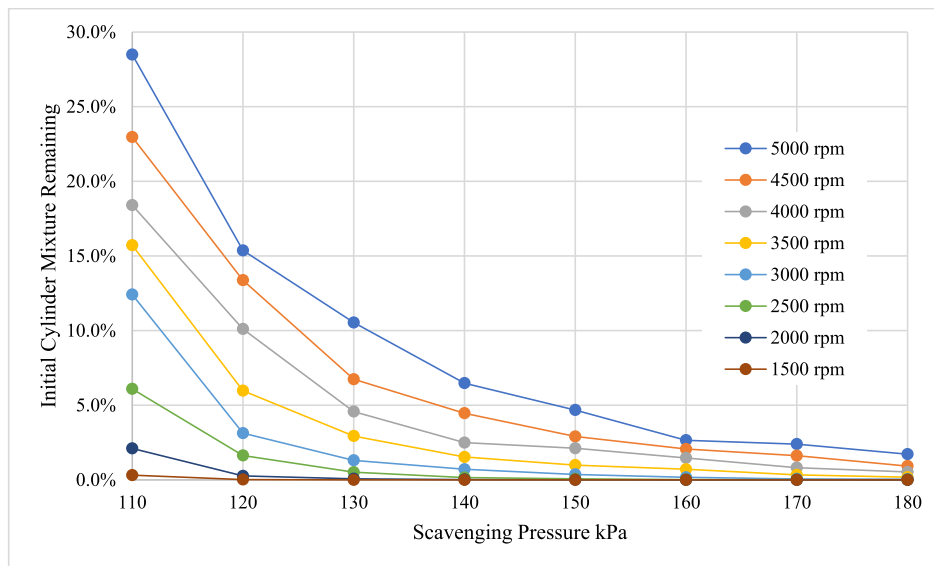**Fig. 11.** 1st Cycle Initial Cylinder Mixture Remaining.

and both k and ε have their own transport equations, which depend on the particular model employed [35]. In the interest of brevity, the reader is referred to appropriate sources for more detail on the k-ε and other RANS/CFD models, including the conservation of energy and other transport equations which are not discussed above [7,35,49,50]. For information on additional conservation laws that are applicable to internal combustion engine simulation, particular attention is drawn to Internal Combustion Engine Fundamentals, 2nd Edition [7], and CONVERGE literature [35].

*2.6. Volume mesh and timestep*

Whilst in these simulations the volume mesh is generated by the solver at runtime, the mesh parameters including base grid size, embedded cells and AMR, need to be appropriately specified. The base

grid size, which affects both AMR and embedded cells, was set at a resolution of 3 mm × 3 mm × 3 mm. Fixed embeddings were specified to seed smaller cells of 0.75 mm on both piston crowns, as well as an arbitrarily defined cylindrical region, which encompasses the engine cylinder and the liner ports. The higher resolution in these areas is important for the geometry sealing (i.e., piston porting) processes [34–36].

AMR (configured using the input file 'amr.in') was enabled based on a velocity gradient of 3 m/s across a cell, with a maximum embedding level of 2 (cell size 0.75 mm) and a maximum cell count of 100,000. Because the fixed embeddings resulted in a cell-count in excess of 100,000 throughout the simulation, AMR would not embed any further [35,46]. However, were it found that excessive velocity gradients (for example, at higher engine speeds and scavenging pressures) caused poor convergence, the 'placeholder amr.in' file meant that AMR could be
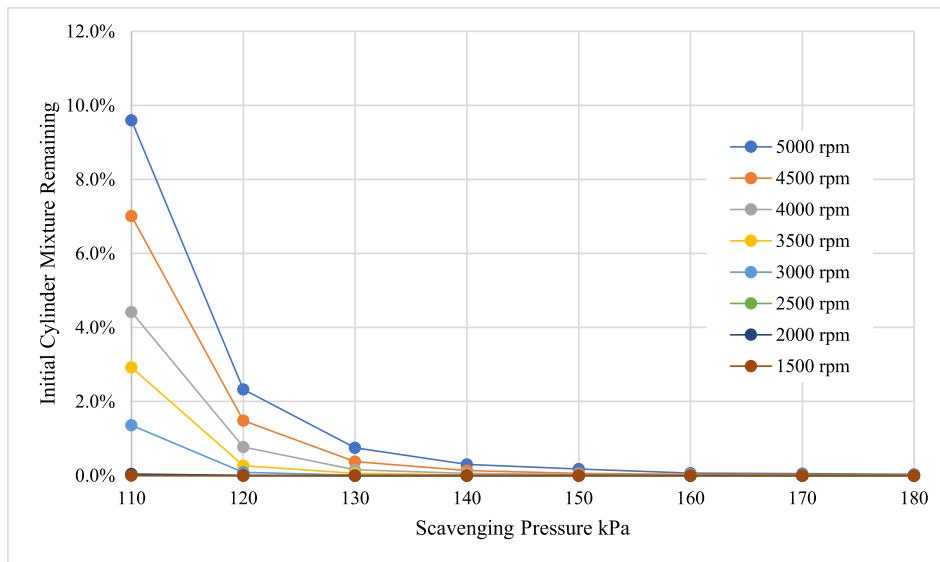
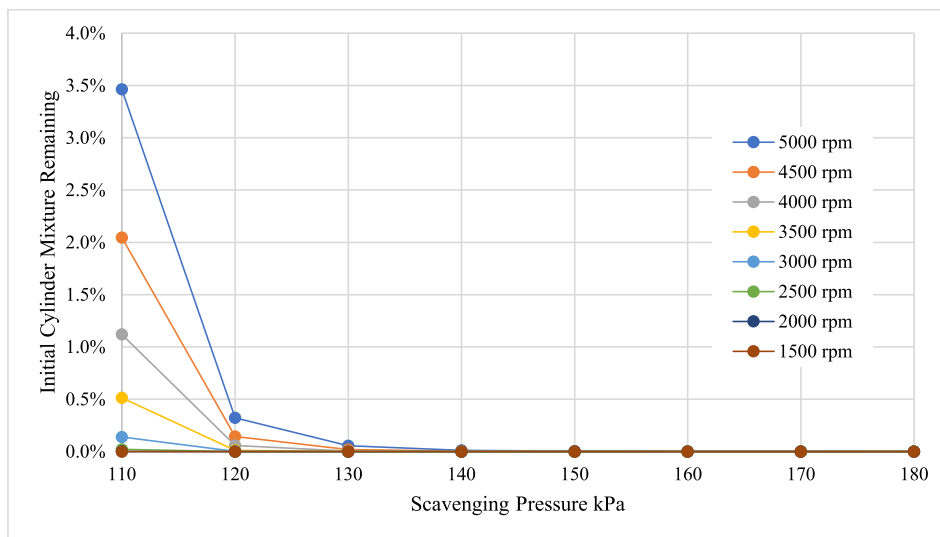Fig. 12. 2nd Cycle Initial Cylinder Mixture Remaining.



Fig. 13. 3rd Cycle Initial Cylinder Mixture Remaining.

activated by simply changing these values and, if necessary, the velocity criterion, without having to re-export the entire case set-up. The maximum timestep was set at 1E-05 s, the minimum timestep 1E-08 [35].

## 3. Simulation results

The following results are collated into data series delineated by engine speed for the first, second and third cycles. The trapped mass of all species in the cylinder is shown on a cycle-by-cycle basis in Fig. 8 through Fig. 10, followed by the remaining percentage of the original in-cylinder species mixture, also on a cycle-by-cycle basis, in Fig. 11 through Fig. 13 [33]. This percentage is in reference to the original trapped mass fraction of $H_2O$ at the start of each simulation as detailed in Table 2, which was kept constant for all simulations, and assumes a homogenous in-cylinder mixture.

The progression of the in-cylinder trapped mass through each cycle highlights some interesting characteristics of the geometry. After the first cycle (which includes the initial blowdown), the trapped mass decreases as engine speed increases at lower scavenging pressures, but it

increases with engine speed at higher scavenging pressures (although there is some crossover of the 4500 rpm and 5000 rpm curves). This behaviour might be explained by the fact that port open time decreases with engine speed, and the initial conditions for all the simulations were the same: Lower scavenge pressures take longer to influence in-cylinder motion and overcome any backflow caused by excess in-cylinder pressure at IPO, especially considering the initially stationary in-cylinder flow field. However at higher engine speeds there is less time for intake backflow to occur after EPC, and (where the scavenge pressure is high enough) the trapped mass increases. Whilst the influence of the initial conditions cannot be ruled out after only one engine cycle, the remaining original in-cylinder mixtures broadly reflect these phenomena: After the first cycle the higher rpm curves indicate that at the lowest scavenge pressures of 110 kPa and 120 kPa, in the region of 15–30 % of the original in-cylinder mass is still present after scavenging, but at 130 kPa scavenging pressure and above the scavenging performance appears to increase with more than 90 % of the original mass cleared except at 5000 rpm.

By the third cycle however, sufficient time has elapsed such that the initial conditions have largely dispersed and the trapped mass increases

**Table 3**
Fuel Table: In-Cylinder Air Mass as a Percentage of Full Speed and Load.

| | | | | | | | | | |
|---|---|---|---|---|---|---|---|---|---|
| **Trapped Air Mass % Full Load** | | | | | | | | | |
| **Full Load Trapped Air Mass in kg:** | | | | | | **0.000158474** | | | |
| | 1.8 | 90.5 | 91.6 | 92.9 | 94.5 | 95.8 | 97.4 | 98.9 | 100.0 |
| | 1.7 | 85.6 | 86.6 | 87.8 | 89.4 | 90.7 | 92.0 | 93.3 | 94.5 |
| | 1.6 | 80.6 | 81.7 | 82.8 | 84.0 | 85.4 | 86.8 | 88.2 | 89.2 |
| | 1.5 | 75.7 | 76.7 | 77.8 | 78.9 | 80.2 | 81.5 | 82.7 | 83.8 |
| **Scavenge Absolute Pressure (Bar)** | 1.4 | 70.8 | 71.8 | 72.7 | 73.8 | 74.9 | 76.1 | 77.3 | 78.5 |
| | 1.3 | 65.9 | 66.8 | 67.6 | 68.6 | 69.7 | 70.8 | 72.0 | 73.0 |
| | 1.2 | 61.0 | 61.7 | 62.6 | 63.4 | 64.5 | 65.5 | 66.6 | 67.5 |
| | 1.1 | 56.1 | 56.8 | 57.5 | 58.3 | 59.2 | 60.0 | 60.5 | 60.7 |
| | | 1500 | 2000 | 2500 | 3000 | 3500 | 4000 | 4500 | 5000 |
| **Engine Speed (RPM)** | | | | | | | | | |
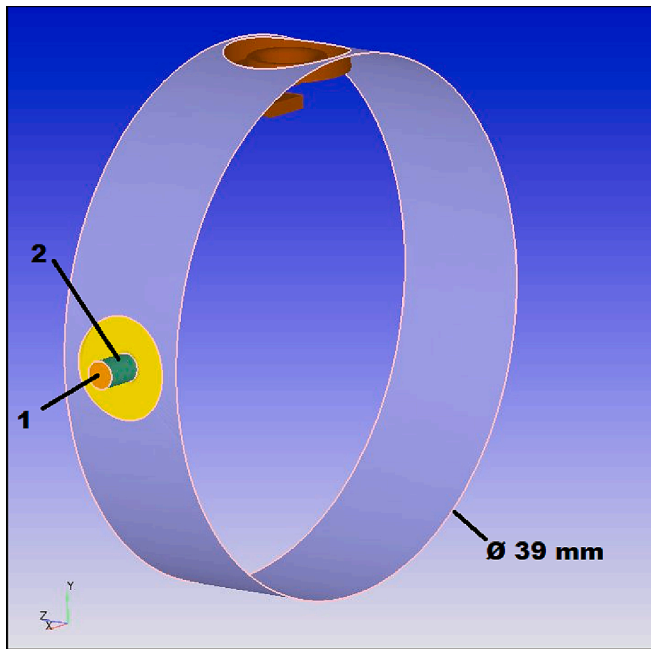


**Fig. 14.** Isolated View of Central Part of Cylinder (purple), with Injector Tip (yellow) and Spark Plug Tip (brown) and Injector Gas Inlet (1) and Injector Tube (2). (For interpretation of the references to colour in this figure legend, the reader is referred to the web version of this article.)

both with scavenge pressure and engine speed. However, for the 5000 rpm curve the drop in trapped mass from 120 kPa to 110 kPa is clearly greater than it is from 130 kPa to 120 kPa. Also, there is in excess of 1 %, 2 % and 3 % of the original trapped mass present at 4000 rpm, 4500 rpm and 5000 rpm respectively at the 110 kPa data point even after three engine cycles, yet less than 0.5 % after three engine cycles above 120 kPa. Such behaviour is not unexpected, since a high engine speed and low scavenge pressure condition in a fuelled engine would be akin to a

throttle being closed in a conventional four-cycle engine, but it may lead to an overestimation of the required fuel as is demonstrated in the following section.

### 3.1. Fuel table

Given that the motored trapped mass values appeared to have largely stabilised after three cycles (Fig. 10), these values were used to generate a 2D array. The maximum speed load point of 5000 rpm and 180 kPa scavenge pressure was used as a reference point, and all the other data points then evaluated against it and expressed as a percentage. The resulting array of trapped air masses effectively generates a 'fuelling table', which is presented in Table 3 and by modifying Eq. (1), and using an appropriate air fuel ratio, any point in Table 3 can be used to approximate the required fuel with Eq. (9):

$$m_{fuel\_x} = \frac{1}{100} * \frac{\%_x}{m_{air_{full}}} * \lambda, \tag{9}$$

where $m_{fuel\_x}$ is the mass of fuel required at datapoint 'x' (in kg), $\%_x$ is the air mass 'percent of full' indicated at that point in Table 3, $m_{air\_full}$ is the full load trapped air mass indicated in Table 3 (in kg), and $\lambda$ is the desired air/fuel ratio; note that 'x' represents a coordinate, described by a speed and a scavenge pressure. This layout reflects one of the approaches sometimes used in an ECU, including a popular aftermarket unit where the values in the fuel table are similarly expressed as a percentage of the full load fuelling requirement [53].

The intrinsic value of Table 3 therefore is that it will significantly aid programming of the ECU fuel table to enable the physical testing of the prototype engine. Without it, because of the unusual nature of the prototype, the lack of any other data would have required a rather more risky approach of simply turning up the fuel until the engine fires, with an additional lack of any guidance on how fuel demand might vary depending on speed and load. However, it was already identified that at high engine speeds and low scavenge pressures the table may tend to over-estimate the fuelling requirements, particularly since in a fuelled engine there will be an exhaust blowdown event during each cycle. In order to evaluate this risk, a series of 9 fuelled simulations were carried

**Table 4**

Fuel Gas Mass Flow Rate for 3000 rpm 150 kPa Fuelled Simulation.

| Timing Crank Angle Degrees | Flowrate kg/s |
|---|---|
| −113 | 0.000000000 |
| −112.9 | 0.000435973 |
| −112.8 | 0.000871947 |
| −112.7 | 0.001307920 |
| −112.6 | 0.001743893 |
| −112.5 | 0.002179866 |
| −112.4 | 0.002615840 |
| −112.3 | 0.003051813 |
| −112.2 | 0.003487786 |
| −112.1 | 0.003923759 |
| −112 | 0.004531008 |
| −84 | 0.004531008 |
| −83.9 | 0.003923759 |
| −83.8 | 0.003487786 |
| −83.7 | 0.003051813 |
| −83.6 | 0.002615840 |
| −83.5 | 0.002179866 |
| −83.4 | 0.001743893 |
| −83.3 | 0.001307920 |
| −83.2 | 0.000871947 |
| −83.1 | 0.000435973 |
| −83 | 0.000000000 |
| **Total Mass kg** | **7.266221E-06** |

**Table 5**

Ignition Energy Sources.

| Source | Size | Location X, Y,Z | Energy | Max Temp. | Timing |
|---|---|---|---|---|---|
| S1-1 | Ø 0.8 mm | 0, 0.01655, 0 | 0.02 Joules | 50,000 K | −30 CAD to −29.5 CAD |
| S1-2 | Ø 0.8 mm | 0, 0.01655, 0 | 0.02 Joules | 50,000 K | −30 CAD to −20 CAD |
| S2-1 | Ø 0.8 mm | 0, 0.01655, 0 | 0.02 Joules | 50,000 K | −15 CAD to −14.5 CAD |
| S2-2 | Ø 0.8 mm | 0, 0.01655, 0 | 0.02 Joules | 50,000 K | −15 CAD to −5 CAD |

out using methane (CH4) as the fuel species.

### 3.1.1. Fuelled simulations

Bearing in mind the computational constraints described in section 2.4, methane was chosen as a fuel because it is the simplest of the alkane fuels and is gaseous [54] (assuming the injector is approximately the same temperature as the cylinder wall), so obviating the need to configure any spray/parcel modelling. Setting the air/fuel ratio to stoichiometric ($\varphi = \lambda = 1$) in Eq. (9) also makes the results easy to compare. The simulation cases run were at 1500 rpm, 3000 rpm and 5000 rpm, at scavenge pressures of 120 kPa, 150 kPa and 180 kPa, to reflect the upper and lower limits of the fuel table. It will be noted that 110 kPa was not modelled; this is because it was already clear from the motored simulations that such a low scavenge pressure is unlikely to provide satisfactory results.

#### 3.1.1.1. Configuration.

Apart from the injector nozzle (and associated tube and inlet), the geometries and boundary conditions are exactly the same as those used for the motored simulations, as are the initial conditions in the intake, cylinder and exhaust regions, the settings for the base grid and fixed embeddings, and the data files for the material properties. The injector nozzle geometry was altered to incorporate a simple tube, located in its own region and with an intake boundary (similar, though not identical, to the air intake boundary) located at the end. The temperature of these additional boundaries was set at 400 K, the same temperature as the cylinder wall, and the initial conditions in the injector region were a species concentration of 100 % CH4 at a pressure of 101325 Pa (atmospheric). Fig. 14 shows the modified injector geometry in the centre of the cylinder; though not identical, the diameter and length of the tube were guided by a hydrogen case from the CONVERGE® example case library, and are 2 mm and 3 mm respectively [34]:

At the injector gas inlet boundary, due to the small diameter of it and the injector tube, the turbulence length scale was reduced by a factor of 10 to 0.3 mm (i.e. below 20 % of the hydraulic diameter, as recommended by CONVERGE®). Also, instead of a fixed pressure being specified, a mass flow-rate profile was specified, over a duration of 30 CAD. Similar to the same hydrogen example case, the profile incorporates an 'on ramp' and 'off ramp' each of which lasts for a duration of 1 CAD; the nominal flowrate occurs for 28 CAD. The mass flowrate for

**Table 6**

Equivalence Ratio and Error Per Cycle.

| Simulation | Phi Target | Phi Actual 1 | Phi % Error 1 | Phi Actual 2 | Phi % Error 2 | Phi Actual 3 | Phi % Error 3 |
|---|---|---|---|---|---|---|---|
| **1500_120** | **1.000** | 0.999 | -0.103% | 1.000 | 0.037% | 0.999 | -0.052% |
| **1500_150** | **1.000** | 0.998 | -0.234% | 1.000 | -0.042% | 0.999 | -0.069% |
| **1500_180** | **1.000** | 0.997 | -0.290% | 0.998 | -0.209% | 0.999 | -0.135% |
| **3000_120** | **1.000** | 1.060 | 5.985% | 1.071 | 7.144% | 1.082 | 8.159% |
| **3000_150** | **1.000** | 1.004 | 0.411% | 1.011 | 1.100% | 1.016 | 1.591% |
| **3000_180** | **1.000** | 1.002 | 0.218% | 1.008 | 0.783% | 1.008 | 0.812% |
| **5000_120** | **1.000** | 1.300 | 29.998% | 1.352 | 35.197% | 1.433 | 43.286% |
| **5000_150** | **1.000** | 1.094 | 9.393% | 1.154 | 15.416% | 1.171 | 17.124% |
| **5000_180** | **1.000** | 1.042 | 4.222% | 1.094 | 9.449% | 1.100 | 9.964% |

**Table 7**
Injected Fuel Mass (kg) and Error Per Cycle.

| Simulation | Required Fuel Mass | Mass Injected 1 | Mass % Error 1 | Mass Injected 2 | Mass % Error 2 | Mass Injected 3 | Mass % Error 3 |
|---|---|---|---|---|---|---|---|
| 1500_120 | 5.617E-06 | 5.630E-06 | 0.237% | 5.638E-06 | 0.375% | 5.638E-06 | 0.378% |
| 1500_150 | 6.977E-06 | 6.991E-06 | 0.209% | 7.003E-06 | 0.373% | 7.003E-06 | 0.372% |
| 1500_180 | 8.334E-06 | 8.351E-06 | 0.201% | 8.364E-06 | 0.366% | 8.365E-06 | 0.374% |
| 3000_120 | 5.845E-06 | 5.860E-06 | 0.261% | 5.869E-06 | 0.399% | 5.869E-06 | 0.412% |
| 3000_150 | 7.266E-06 | 7.283E-06 | 0.227% | 7.295E-06 | 0.394% | 7.294E-06 | 0.389% |
| 3000_180 | 8.706E-06 | 8.725E-06 | 0.215% | 8.740E-06 | 0.391% | 8.739E-06 | 0.383% |
| 5000_120 | 6.215E-06 | 6.232E-06 | 0.284% | 6.240E-06 | 0.404% | 6.243E-06 | 0.455% |
| 5000_150 | 7.725E-06 | 7.744E-06 | 0.240% | 7.767E-06 | 0.549% | 7.764E-06 | 0.507% |
| 5000_180 | 9.214E-06 | 9.234E-06 | 0.219% | 9.252E-06 | 0.418% | 9.254E-06 | 0.439% |
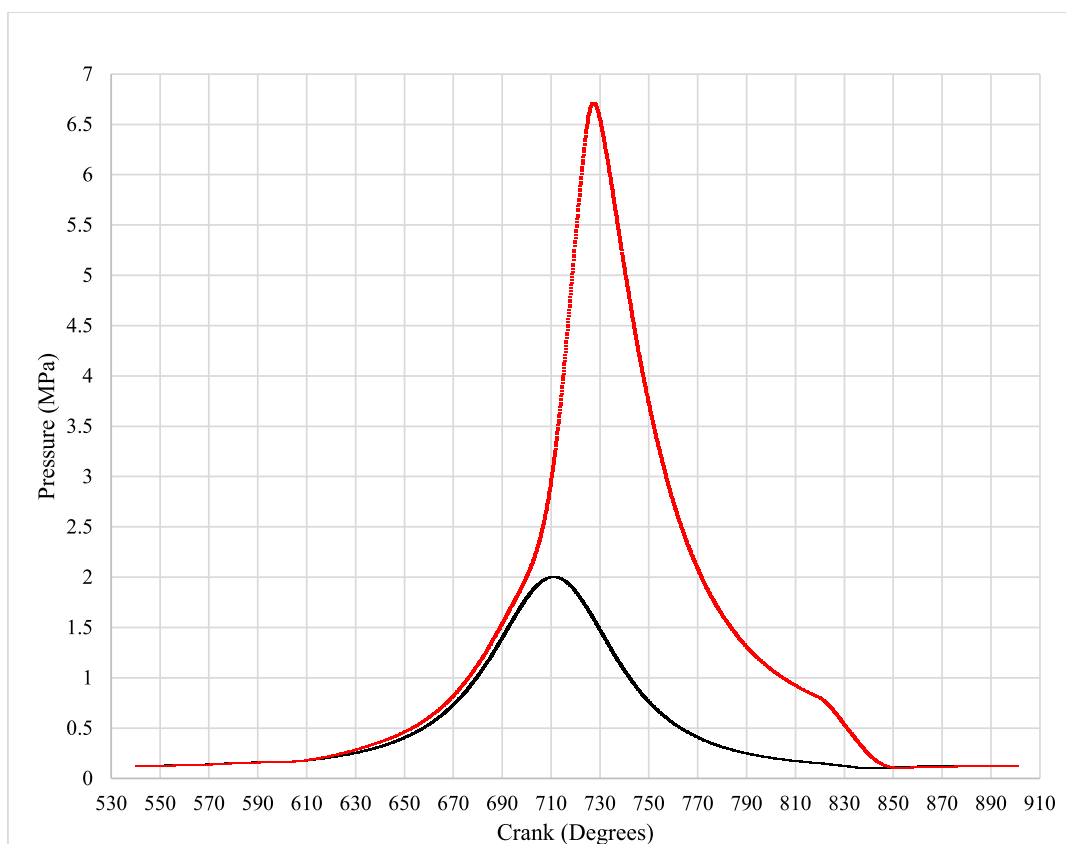


**Fig. 15.** In-Cylinder Pressure Tracing for Motored Case (Black Line) and Fuelled Case (Red Line). (For interpretation of the references to colour in this figure legend, the reader is referred to the web version of this article.)

3000 rpm, 150 kPa is shown below in Table 4 as an example [34].

The nominal flowrate, in this case 0.004531008 kg/s, incorporates a correction factor to account for the mass injected during the on and off ramps, such that over the whole injection profile the total mass ('Total Mass kg' in Table 4) is exactly equal to the required fuel specified. Note that the flowrates are all in kg/s and not kg/CAD. Because the injector internals are located in their own region, the flow between this 'injector' region and the cylinder region is switched on at −115 CAD to allow the mass flowrate at the injector inlet to flow into the cylinder, and off at −85 CAD. This is shortly before and after the timing of the mass flow
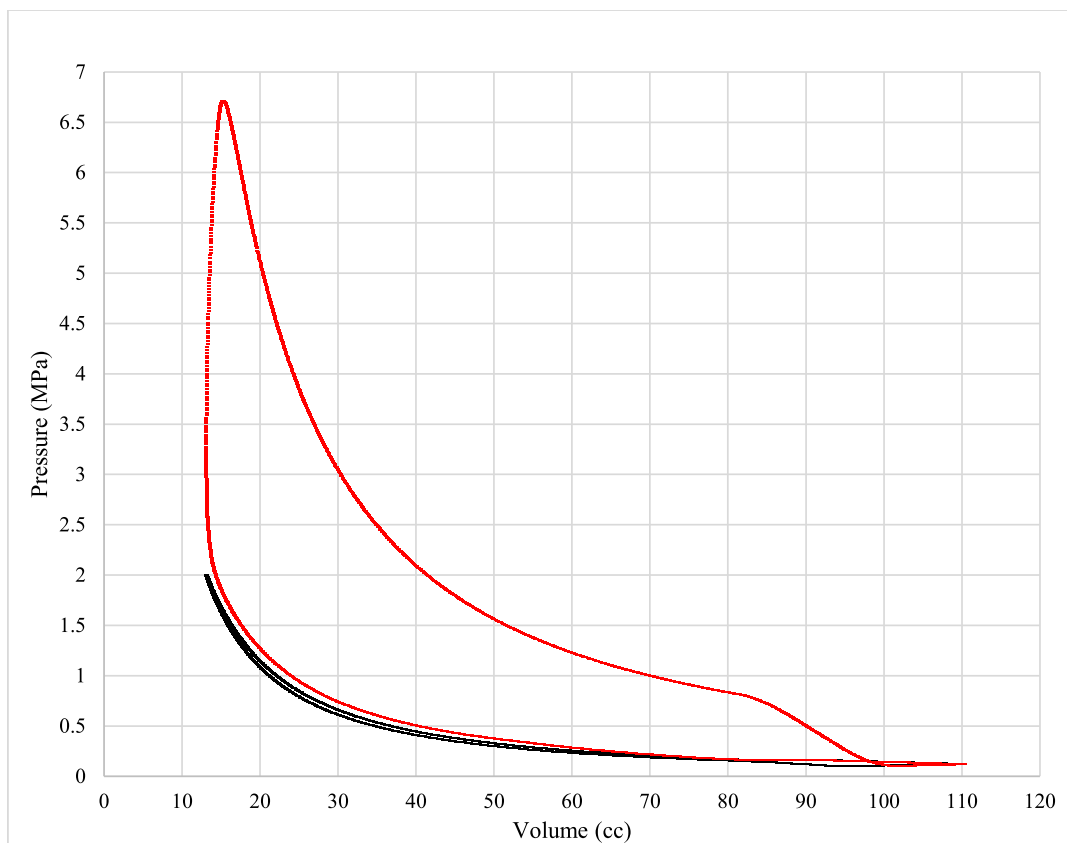
**Fig. 16.** Pressure Volume Graph for the Motored Case (Black Line) and Fuelled Case (Red Line). (For interpretation of the references to colour in this figure legend, the reader is referred to the web version of this article.)
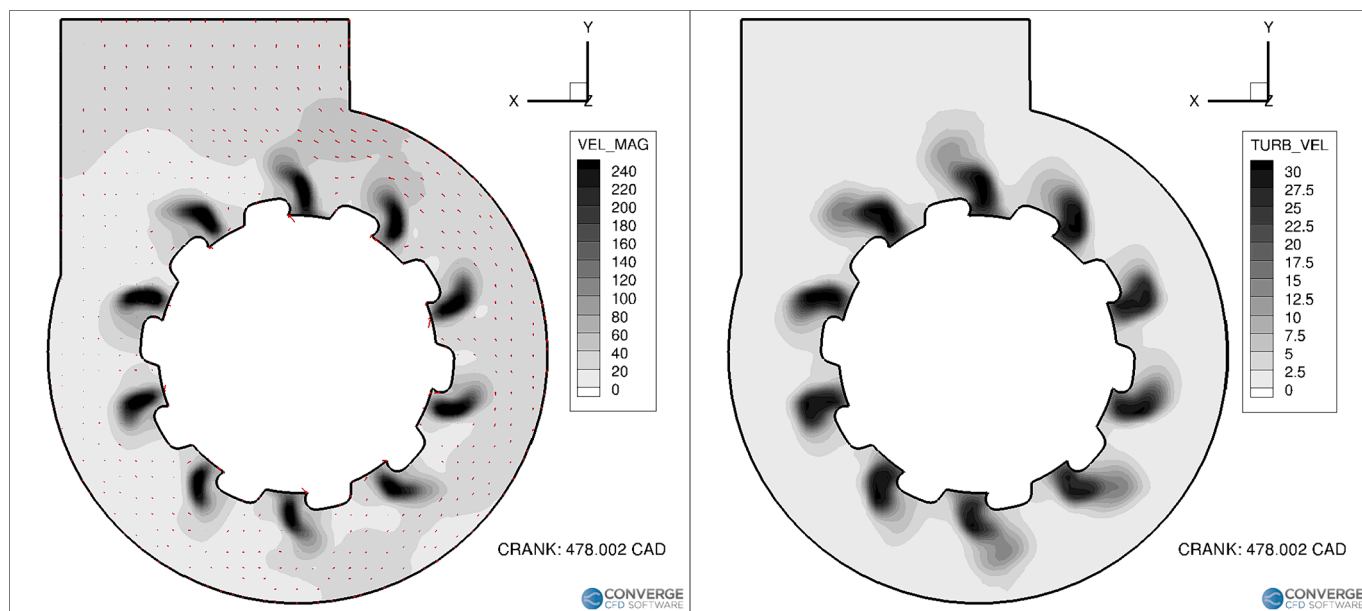


**Fig. 17.** Intake Velocity Magnitude (m/s) and Turbulent Velocity (m/s), Simulation Time 478 CAD.

rate profile to allow pressure equalisation before, and more time for any residual fuel gas in the injector tube to enter the cylinder after 'injection'. The ignition timing was kept constant for all the simulation cases at −30 CAD, and the SAGE detailed chemistry solver (for more details of which the reader is referred to CONVERGE® literature) was used for combustion simulation. This was set to run only around the time of combustion to reduce computation time, with CH4 set as the fuel species and ignition initiated through the addition of two spherical energy sources in the spark plug gap. The use of two heat sources reflects the initial discharge and afterglow of an electrical spark, and together these raise the temperature locally above the specified combustion cut-off temperature of 600 K; Table 5 details the ignition source volumes [46]:
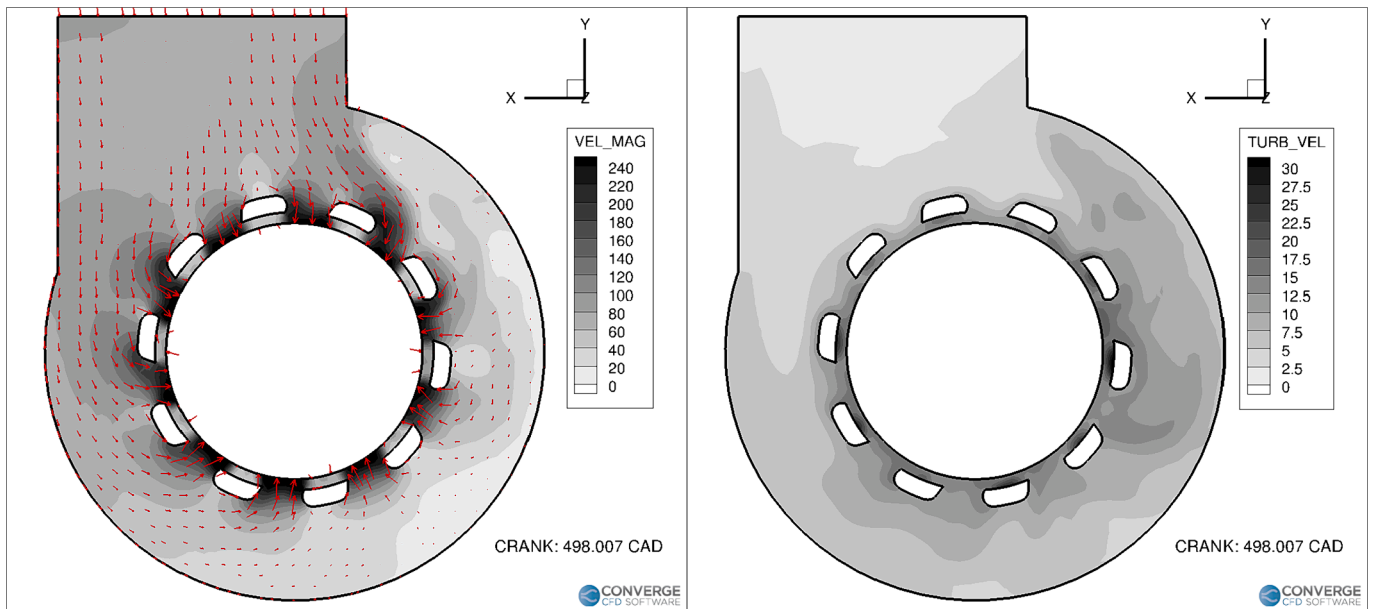
**Fig. 18.** Intake Velocity Magnitude (m/s) and Turbulent Velocity (m/s), Simulation Time 498 CAD.
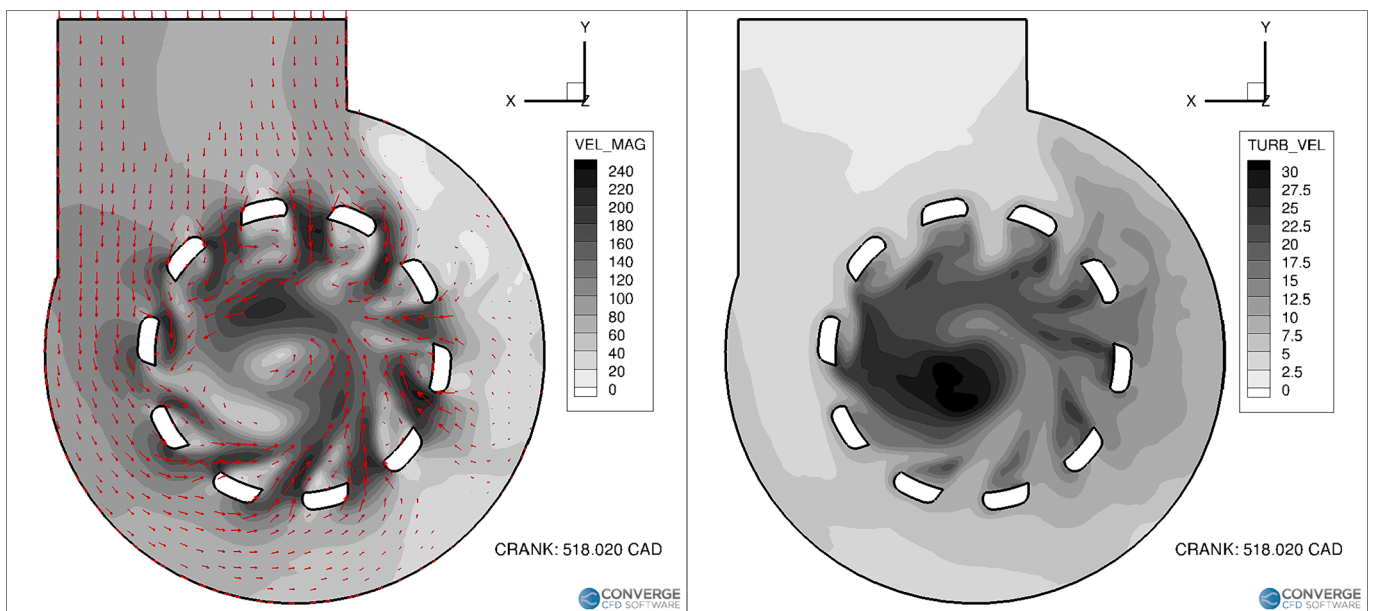


**Fig. 19.** Intake Velocity Magnitude (m/s) and Turbulent Velocity (m/s), Simulation Time 518 CAD.

For reference, coordinate X,Y,Z = 0,0,0 represents the location of the axial and radial centre of the cylinder. Sources S2-1 and S2-2 represent a secondary spark, added for the eventuality that the first spark failed to ignite the mixture.

Settings for AMR were mostly unchanged with the velocity criterion remaining the same throughout at 3 m/s across a cell with a maximum embedding level of 2 (cell size 0.75 mm). However, from −31 CAD to 60 CAD the maximum cell count was increased to 250,000 from 100,000 and an additional embedding criterion added based on a temperature gradient of 2.5 K across a cell, with a maximum embedding level of 4 (cell size 0.1875 mm). This was to accommodate the smaller length scales associated with the early stages of combustion and reduce any grid-induced diffusive errors [46]. Furthermore, the maximum timestep was reduced from 1E-05 s to 5E-06 s from −31 CAD to 105 CAD to avoid stability issues; the minimum timestep was left intact.

It is prudent at this point to re-emphasise that the *primary* objective of this work is not to serve as an evaluation of the performance of the engine geometry and configuration by, for example, generating a realistic in-cylinder PV plot. Rather, it is to solve an engineering problem by generating and testing a fuel table that is of sufficient accuracy so as to guide the setup and physical engine testing of a novel prototype, for which there are at the time of writing, no empirical results. Therefore, provided they do not cause the simulation to become unstable, things like grid-induced diffusive errors, early or late ignition timing, or the velocity of gases in the injector, are not of great concern. This is because even if they may contribute to an over- or under-estimated MPRR and PFP in the cylinder, the simulated combustion processes are solely intended to achieve a moving in-cylinder flow field and exhaust blow-down for each engine cycle. This provides the opportunity to evaluate how closely the bulk in-cylinder equivalence ratio reflects what it *should*
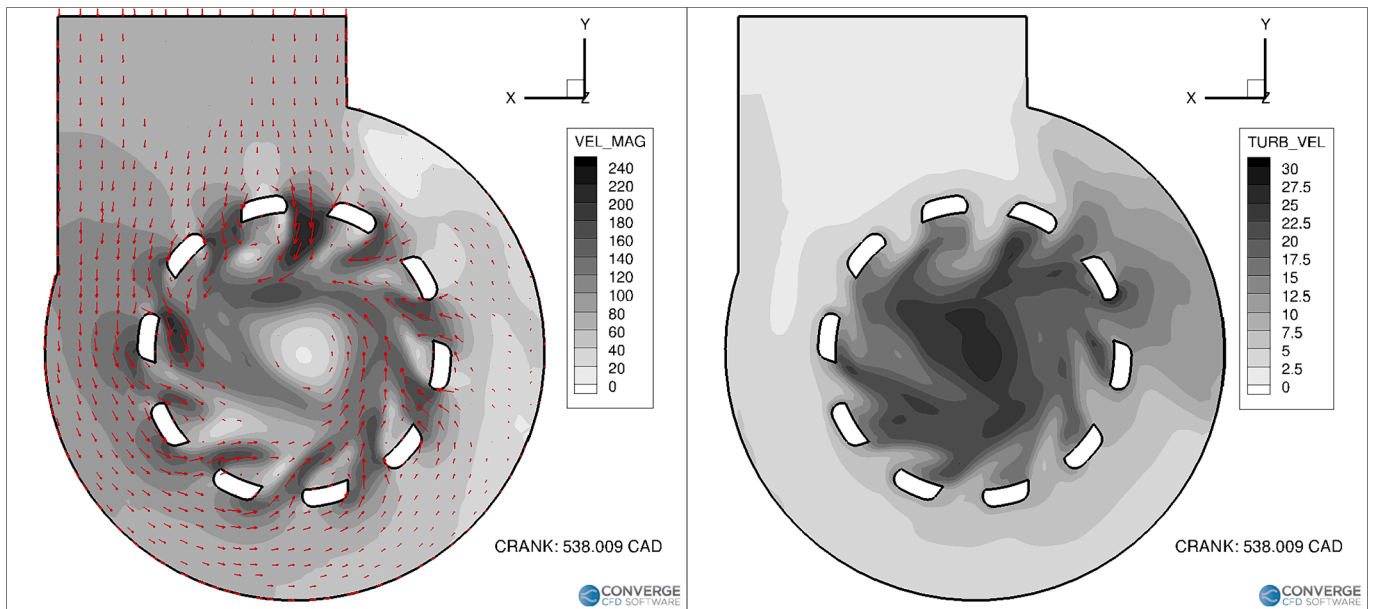
**Fig. 20.** Intake Velocity Magnitude (m/s) and Turbulent Velocity (m/s), Simulation Time 538 CAD.
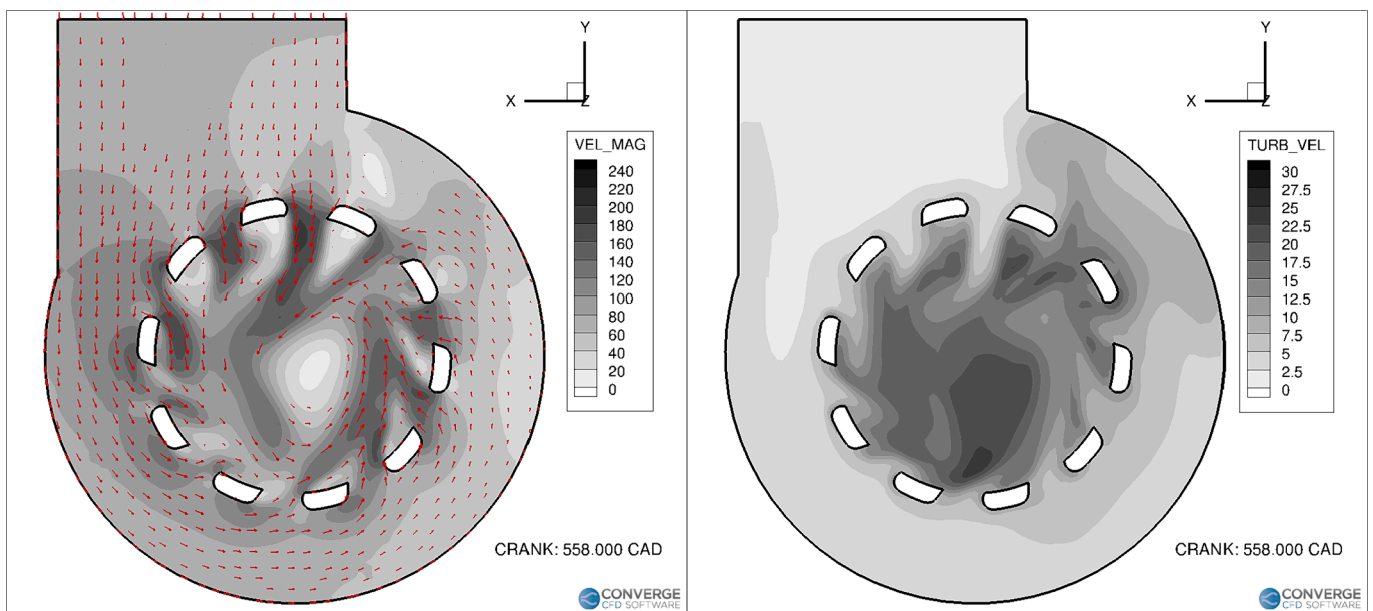


**Fig. 21.** Intake Velocity Magnitude (m/s) and Turbulent Velocity (m/s). Simulation Time 558 CAD.

be if the fuel table (Table 3) is accurate, especially considering the discussion associated with Fig. 8 through Fig. 13 in section 3. The following section lists the results from the fuelled cases, as well as an overview of the OP2S engine cycle and the way in which a bulk swirling motion is generated in the cylinder.

*3.1.1.2. Fuelled simulation results.* The air/fuel equivalence ratio is given for the first, second and third cycles in Table 6, followed by the mass of fuel injected per cycle in Table 7, all at −50 CAD before IDC for each cycle. Note that the mass injected per cycle reflects the data for the total mass flow between the injector region and the cylinder region, and not the mass flow through the injector gas inlet boundary.

The values in Table 6 are encouraging, except for high engine speed and low scavenge pressure conditions. The cells in both Table 6 and Table 7 are coloured according to the percentage error between the

target value, and the actual value: ±0 % to 5 % is dark green, ±5 % to 10 % is light green, ±10 % to 15 % is yellow, ±15 % to 20 % is orange, and greater than ±20 % is red. As discussed earlier for the motored simulations, a high engine speed but low scavenge pressure condition is akin to the throttle being closed in a conventional four-cycle engine, and this was reflected in how well the scavenge pressure was able (or otherwise) to clear the initial in-cylinder conditions. The same characteristics are seen with the fuelled simulations, where there is a significant overestimation of the required fuel for the 5000 rpm 120 kPa case of approximately 30 % for the first cycle, 35 % for the second cycle, and 43 % for the third cycle: The increasing equivalence ratio in Table 6 despite the relatively consistent injected mass in Table 7 is indicative of the cylinder not being fully flushed. At 5000 rpm and 150 kPa, this behaviour is still visible but to a much lesser extent. However, by 5000 rpm 180 kPa (full speed/load) it has mostly disappeared. Furthermore,
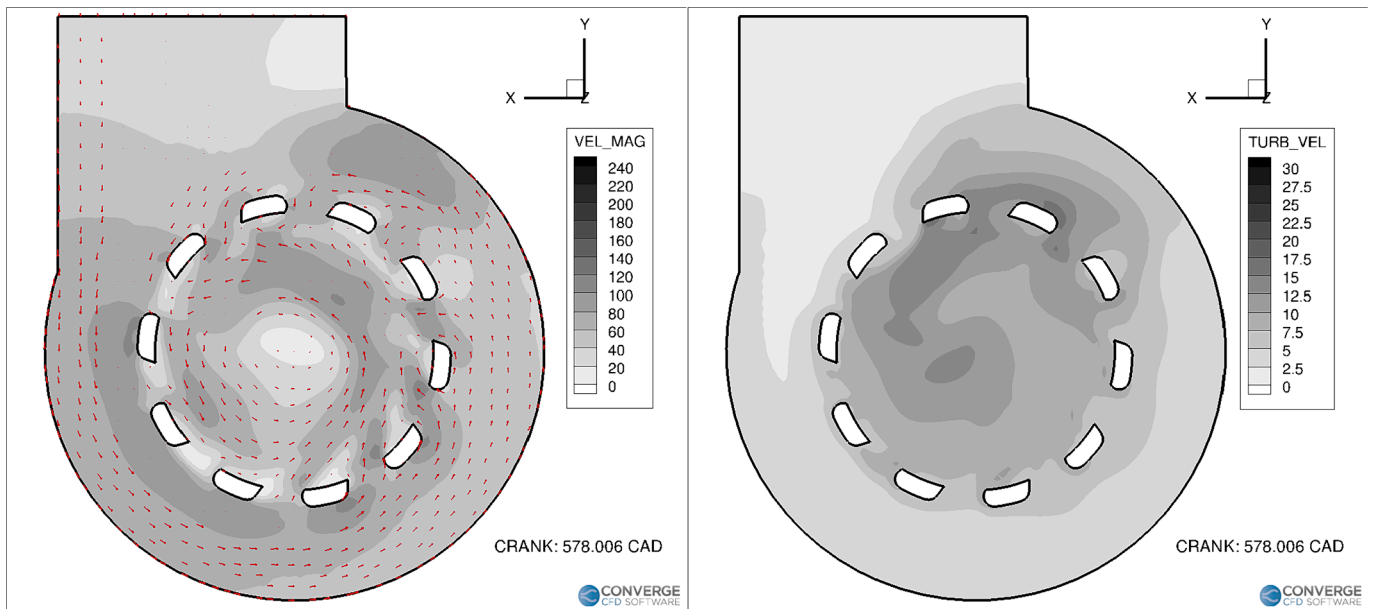
**Fig. 22.** Intake Velocity Magnitude (m/s) and Turbulent Velocity (m/s), Simulation Time 578 CAD.
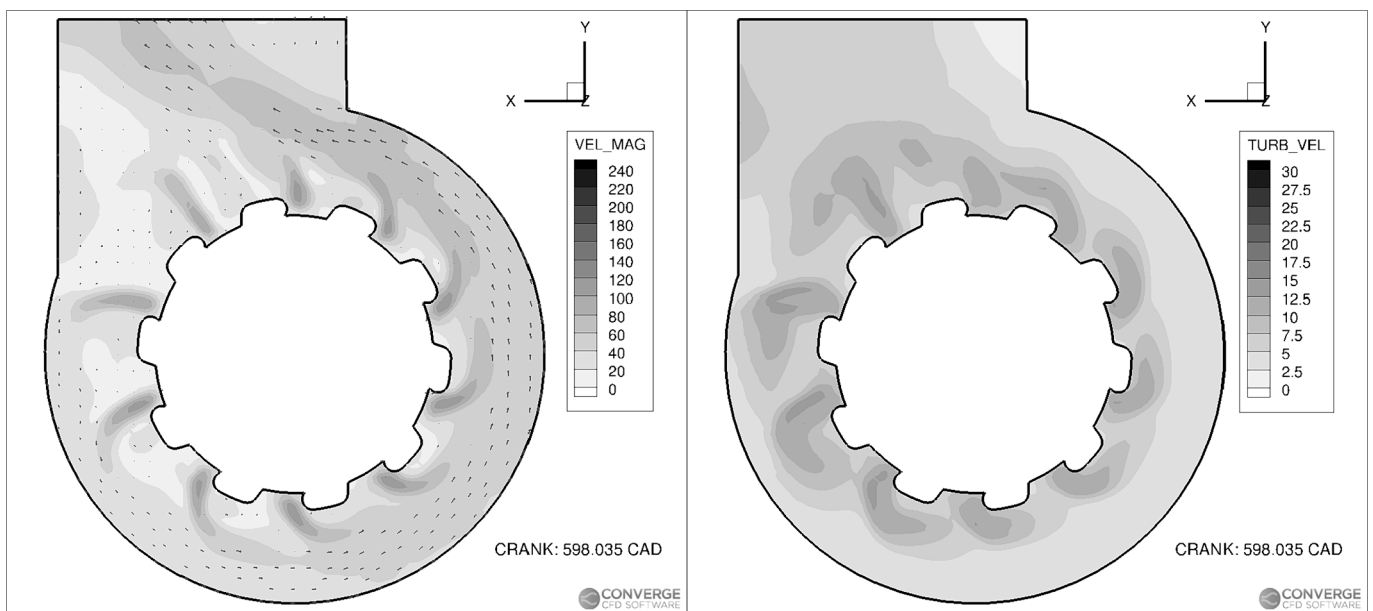


**Fig. 23.** Intake Velocity Magnitude (m/s) and Turbulent Velocity (m/s), Simulation Time 598 CAD.

the results of the 1500 rpm and 3000 rpm fuelled simulations suggest that the motored simulations were able to predict the trapped mass quite well at low to medium engine speeds, given that only the 3000 rpm 120 kPa case had an equivalence ratio error in the $\pm 5$ % to 10 % region, and all the other cases were within $\pm 2$ % error. In all cases the injected mass was well within 1 % of the required fuel mass throughout.

Fig. 15 shows a pressure graph for the third cycle of the 3000 rpm 150 kPa motored simulation case, as well as the 3000 rpm 150 kPa fuelled simulation case:

Whilst the PFP and MPRR should not be viewed as indicative of real-world performance (not least because a pressure tracing like this in a gasoline-fuelled engine would be suggestive of spark knock [7]), the rate and amount of reduction in pressure before EPO (approx. 820 CAD) highlights the increased expansion rate of two pistons over one. A higher stroke to bore ratio typically improves engine efficiency, but it is not

always practical to achieve in four-cycle engines due to the corresponding increase in mean piston speed. Yet by splitting the stroke between two pistons the OP2S architecture can achieve a high stroke to bore ratio, without increasing the mean piston speed [14]. Fig. 16 shows the same data as a PV graph, the difference between the OP2S cycle and the four-stroke cycle is further evidenced through the lack of any visible pumping loop: In a four-cycle engine this would appear as an additional smaller loop at lower pressures, and roughly from maximum to minimum volume [7].

This pumping loss does not appear on the OP2S PV graph because the pumping work is decoupled from piston motion, and in the case of the prototype is driven by an external scavenging blower. As discussed early on, whilst the scavenge pump represents a parasitic load, the decoupling of pumping work from piston motion offers a further degree of control and scope to improve engine efficiency over conventional engines
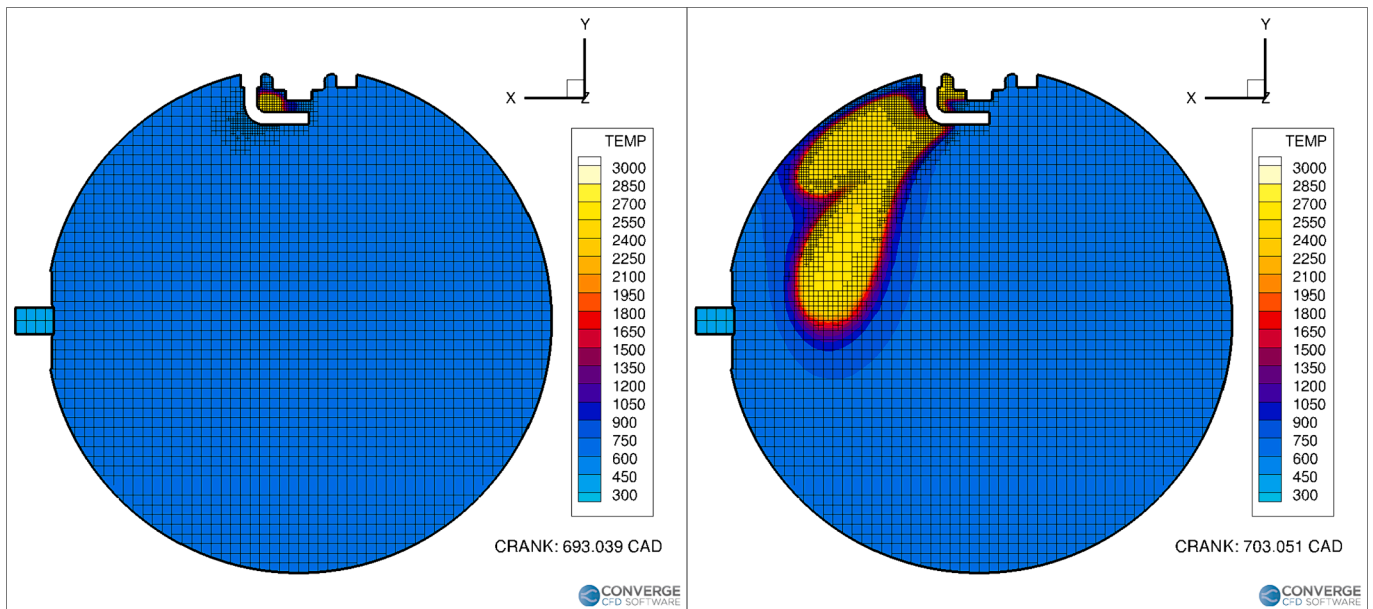
**Fig. 24.** Centre Temperature Contour at 693 CAD (left) and 703 CAD (right), in Kelvin.
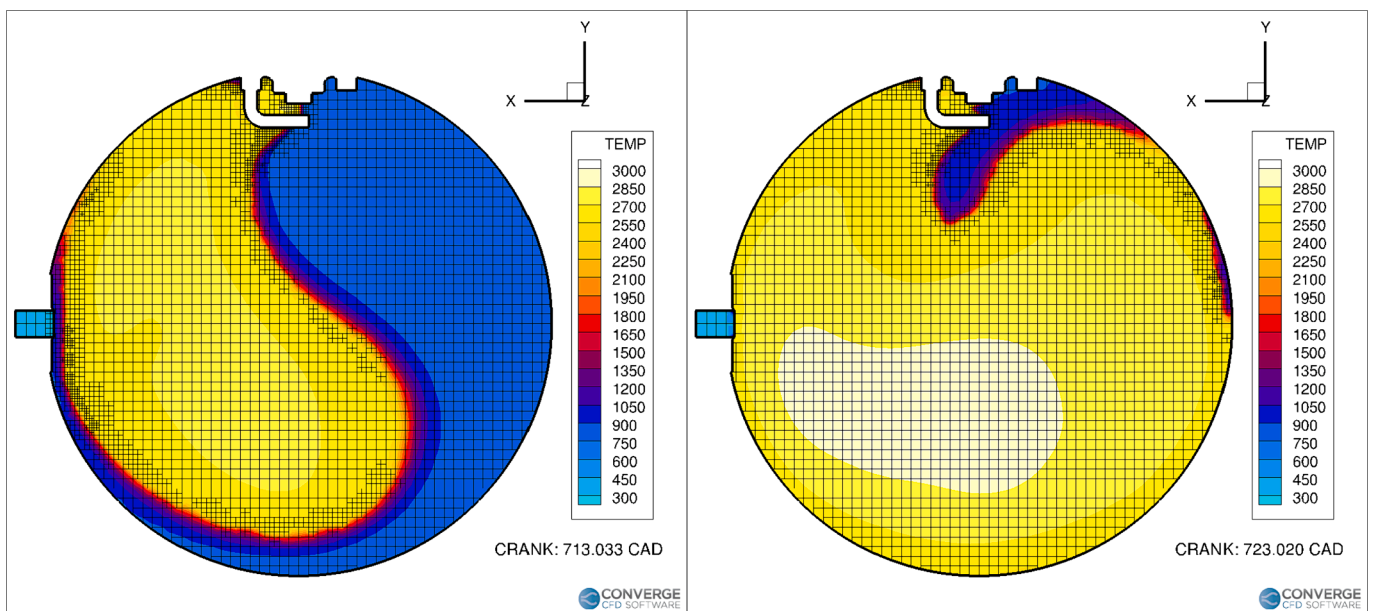


**Fig. 25.** Centre Temperature Contour at 713 CAD (left) and 723 CAD (right), in Kelvin.

[13,15].

Fig. 17 through Fig. 23 show cross sections through the middle of the intake gallery from the intake end of the cylinder, to illustrate the swirling motion that the gallery and liner ports help to establish. Velocity magnitude is shown on the left, with 3-dimensional vectors indicating the direction. These vectors scale with intensity, and are configured as 'head at point'. Those vectors that either appear as dots or are not visible at all either mean the z component of velocity is dominant, or the velocity magnitude is much lower. Turbulent velocity is shown on the right. The scales of both contours have been constrained to improve contrast [33].

In Fig. 17 the initial backflow into the intake can be observed shortly after IPO; the cylinder itself is not yet visible here or in Fig. 18 because the piston crown has not traversed the middle of the ports where the cross section is located. By Fig. 19, the piston crown has cleared the

middle of the ports, and the angled ports coupled with the offset intake gallery inlet begin to establish a bulk counterclockwise swirling regime in the cylinder, but with very high velocities slightly above the cylinder centreline – recall that the velocity is 3 dimensional and gases flow along the length of the cylinder as well as swirling around it. The right-hand side of Fig. 19 also indicates a high degree of turbulence close to the centre, whereas by Fig. 20 this is less apparent, and the bulk swirling motion more well developed. Here, this motion is better aligned with the centre of the cylinder, as it is likewise in Fig. 21. By Fig. 22, the returning piston crown has crossed the middle of the ports with the residual flow in the intake gallery circulating counterclockwise until Fig. 23, where there is a brief intake backflow. This is likely caused by a modest pumping effect due to the decreasing cylinder volume as the pistons approach one-another.

The generation of a bulk swirling motion in the cylinder is intended

not only to improve the mixing of fuel and air, but also to mitigate against the large flame propagation distance from the spark plug to the other side of the cylinder by encouraging the flame to 'wrap around' the combustion chamber, which is formed chiefly by the two piston crowns. The obvious trade-off is the proximity of the flame to the liner, where more heat could be lost to coolant and impact efficiency. However, were this not the case and the flame front allowed to progress radially from the spark plug, the increasing pressure of the unburned mixture/end gas would likely cause it to slowdown as it approaches the other side of the cylinder [7]. Fig. 24 and Fig. 25 show temperature contours of the central slice of the cylinder, beginning shortly after SOC. Here, the mesh has been included to highlight the smaller cells that AMR has embedded due to the large temperature gradient between the burned and unburned mixtures [33]:

Though not intended as an evaluation of the performance of the engine, the general characteristics of the intake cross sections and the above temperature contours suggest that the intake liner ports and gallery have the desired effect. More importantly however, the fuel table (Table 3) provided sufficiently accurate results to be able to configure the fuelled simulations to work first time for the majority of the conditions tested. Therefore, whilst high speed and low scavenge pressure conditions are expected to be more challenging, it is likely to save significant time when configuring the ECU of the prototype engine, given the absence of any empirical data for the novel design.

## 4. Conclusions

The opposed-piston two-stroke engine possesses inherent thermodynamic advantages over other engine architectures, is well proven in compression ignition form, and presents a significant opportunity to aid in the quest to reduce anthropogenic GHG emissions. It is worth noting that the literature on spark ignition opposed piston engines remains less prevalent, particularly in the case of blower-scavenged examples. Extending the advantages of the OP2S architecture to utilise fuels better suited to spark ignition, such as hydrogen or methane, could represent a further opportunity to reduce GHG emissions. In this work, a series of 3-dimensional computational fluid dynamics simulations were performed to estimate the fuelling requirements of a novel, blower-scavenged SI OP2S engine prototype that is currently under construction. By configuring the trapped air mass results into a fuel-agnostic table that needs only the air fuel ratio to return an estimate for required fuelling, significant time could be saved programming the fuel map of the ECU, especially given that there currently exist no empirical fuelling data for the prototype.

Targeted testing of datapoints in the table using fuelled simulations suggests that whilst at higher engine speeds and lower scavenge pressures (5000 rpm, 120/150 kPa) it could over-predict the required fuel, at all the other tested conditions it was able to predict the required fuel within approximately ±10 %, including 5000 rpm, 180 kPa. This is particularly true at low to medium engine speeds where at 1500 rpm, 120/150/180 kPa and 3000 rpm, 150/180 kPa it was consistently within 2 % error according to the fuelled simulations, and within 10 % at 3000 rpm, 120 kPa.

Although both the motored and fuelled simulations were not intended as a tool to evaluate the engine performance, they provided some useful characteristics of the engine geometry. In addition to confirming the tendency for reduced scavenging performance at higher engine speeds and lower scavenging pressures, they showed that the swirling intake port geometry has the desired effect, causing a bulk swirling motion within the cylinder that may help fuel mixing. Importantly, it also encourages the flame front to 'wrap around' the cylinder circumference, rather progress only radially, which helps mitigate the large flame propagation distance from the spark plug to the other side of the cylinder.

Based upon these results therefore, the prospect for the successful testing of the novel prototype engine that is under construction appears encouraging.

## CRediT authorship contribution statement

**S.F. Furze:** Writing – original draft, Methodology, Investigation, Formal analysis, Conceptualization. **S. Barraclough:** Writing – review & editing, Formal analysis. **D. Liu:** Writing – review & editing, Supervision. **S. Melendi-Espina:** Writing – review & editing, Supervision, Project administration, Funding acquisition.

## Declaration of competing interest

The authors declare that they have no known competing financial interests or personal relationships that could have appeared to influence the work reported in this paper.

## Data availability

No data was used for the research described in the article.

## References

[1] Kalghatgi G. Is it the end of combustion and engine combustion research? Should it be? Transport Eng 2022;10:100142. https://doi.org/10.1016/j.treng.2022.100142.

[2] BP Statistical Review of World Energy 2022; 2022. https://www.bp.com/content/dam/bp/business-sites/en/global/corporate/pdfs/energy-economics/statistical-review/bp-stats-review-2022-full-report.pdf [accessed April 20, 2023].

[3] Leach F, Kalghatgi G, Stone R, Miles P. The scope for improving the efficiency and environmental impact of internal combustion engines. Transport Eng 2020;1:100005. https://doi.org/10.1016/j.treng.2020.100005.

[4] Senecal PK, Leach F. Diversity in transportation: Why a mix of propulsion technologies is the way forward for the future fleet. Results in Eng 2019;4:100060. https://doi.org/10.1016/j.rineng.2019.100060.

[5] Burton T, Powers S, Burns C, Conway G, Leach F, Senecal K. A Data-Driven Greenhouse Gas Emission Rate Analysis for Vehicle Comparisons. 14–12-01–0006 SAE Int J Electrified Vehicles 2022;12. https://doi.org/10.4271/14-12-01-0006.

[6] Duarte Souza Alvarenga Santos N, Rückert Roso V, Teixeira Malaquias AC, Coelho Baêta JG. Internal combustion engines and biofuels: Examining why this robust combination should not be ignored for future sustainable transportation. Renewable Sustainable Energy Rev 2021;148:111292. https://doi.org/10.1016/j.rser.2021.111292.

[7] Heywood J. Internal combustion engine fundamentals 2E, McGraw Hill LLC; 2018. https://books.google.co.uk/books?id=OmJUDwAAQBAJ.

[8] Van Basshuysen R, Schaefer F. Internal combustion engine handbook. Warrendale, Pa: SAE International; 2016. https://search.ebscohost.com/login.aspx?direct=true&AuthType=sso&db=nlebk&AN=1879561&site=eds-live&scope=site.

[9] Conway G, Joshi A, Leach F, García A, Senecal PK. A review of current and future powertrain technologies and trends in 2020. Transport Eng 2021;5:100080. https://doi.org/10.1016/j.treng.2021.100080.

[10] Westport and Scania Announce Impressive Test Results of H₂ HPDI™ Fuel System for Heavy-Duty Transport, Westport Fuel Systems (n.d.). https://investors.wfsinc.com/news/news-details/2022/Westport-and-Scania-Announce-Impressive-Test-Results-of-H-HPDI-Fuel-System-for-Heavy-Duty-Transport/default.aspx [accessed January 24, 2023].

[11] Fiore M, Magi V, Viggiano A. Internal combustion engines powered by syngas: A review. Appl Energy 2020;276. https://doi.org/10.1016/j.apenergy.2020.115415.

[12] Lhuillier C, Brequigny P, Contino F, Mounaïm-Rousselle C. Experimental study on ammonia/hydrogen/air combustion in spark ignition engine conditions. Fuel 2020;269:117448. https://doi.org/10.1016/j.fuel.2020.117448.

[13] Herold RE, Wahl MH, Regner G, Lemke JU, Foster DE. Thermodynamic benefits of opposed-piston two-stroke engines. SAE Technical Papers 2011. https://doi.org/10.4271/2011-01-2216.

[14] Regner G, Salvi A, Fromm L, Redon F. The opposed-piston engine: The next step in vehicle efficiency. VDI Ber 2016;2016:101–29.

[15] Naik S, Johnson D, Koszewnik J, Fromm L, Redon F, Regner G, et al. Practical applications of opposed-piston engine technology to reduce fuel consumption and emissions. SAE Technical Papers 2013;12. https://doi.org/10.4271/2013-01-2754.

[16] Chown D, Koszewnik J, MacKenzie R, Pfeifer D, Callahan B, Vittal M, et al. Achieving ultra-low oil consumption in opposed piston two-stroke engines. SAE Technical Papers 2019-Janua 2019. https://doi.org/10.4271/2019-01-0068.

[17] Salvi A, Hanson R, Zermeno R, Regner G, Sellnau M, Redon F. Initial results on a new light-duty 2.7L opposed-piston gasoline compression ignition multi-cylinder engine. In: ASME 2018 Internal Combustion Engine Division Fall Technical Conference; 2018. https://doi.org/10.1115/ICEF2018-9610.

[18] US Army awards Cummins $87M contract to deliver the opposed-piston Advanced Combat Engine, Green Car Congress; 2021. https://www.greencarcongress.com/2021/08/20210803-ace.html [accessed February 27, 2023].

[19] Opposed-Piston Heavy-Duty Diesel Engine Performance and Emissions Summary, Achates Power Website; 2023. https://achatespower.com/wp-content/uploads/2023/11/Heavy-Duty-Diesel-Engine-Performance-and-Emissions-Summary.pdf [accessed December 15, 2023].

[20] Hydrogen Opposed Piston Engine Working Group; 2022. https://www.h-ope-wg.com/ [accessed January 21, 2023].

[21] Fromm L. Hydrogen opposed piston engines, Achates Power; 2021. https://achatespower.com/wp-content/uploads/2021/05/Hydrogen-Opposed-Piston-Engines.pdf [accessed January 25, 2023].

[22] Huo M, Sapkal D, El-Hannouny E. Hydrogen Opposed-Piston Engine with Direct Injection, Compression Ignition Combustion, Achates Power Technical Papers; 2023. https://achatespower.com/wp-content/uploads/2023/11/Hydrogen-Opposed-Piston-Engine-with-Direct-Injection-Compression-Ignition-Combustion.pdf [accessed November 24, 2023].

[23] A Horizontally Opposed Two-Stroke Engine. The Motor Cycle; 1914. https://archive.org/details/motorcycle132lond_/page/n285/mode/1up?view=theater [accessed April 21, 2023].

[24] Pirault JP, Flint MLS. Opposed piston engines: evolution, use, and future applications. SAE Int 2009. https://books.google.co.uk/books?id=jXJ0EAAAQBAJ.

[25] Ma F, Zhang J, Wang F. Knock combustion characteristics of an opposed-piston two-stroke gasoline engine. Energy Sci Eng 2022;10:4626–39. https://doi.org/10.1002/ese3.1293.

[26] Ma F, Yang W, Xu J, Li Y, Zhao Z, Zhang Z, et al. Experimental investigation of combustion characteristics on opposed piston two-stroke gasoline direct injection engine. Energies (Basel) 2021;14. https://doi.org/10.3390/en14082105.

[27] Pattakos M, Pattakos E, Pattakou P, Pattakos E. Connecting rod valve, 9303637B2; 2014.

[28] Gao J, Tian G, Jenner P, Burgess M, Emhardt S. Preliminary explorations of the performance of a novel small scale opposed rotary piston engine. Energy 2020;190. https://doi.org/10.1016/j.energy.2019.116402.

[29] Wu L, Feng H, Zhang Z, Jia B, Wang J, Yang F, et al. Experimental analysis on the operation process of opposed-piston free piston engine generator. Fuel 2022;325. https://doi.org/10.1016/j.fuel.2022.124722.

[30] Our Technology - INNEngine, INNEngine Website; 2022. https://innengine.com/our-technology/ [accessed April 20, 2023].

[31] Heavy-Duty Diesel Demonstration Program Review, Achates Power; 2022. https://achatespower.com/wp-content/uploads/2022/06/Achates-Power-HD-Demo-Technical-Review-May-4-2022.pdf [accessed February 27, 2023].

[32] Stępień Z. A comprehensive overview of hydrogen-fueled internal combustion engines: Achievements and future challenges. Energies (Basel) 2021;14. https://doi.org/10.3390/en14206504.

[33] Richards KJ, Senecal PK, Pomraning E. Converge 3.0 2021.

[34] Richards KJ, Senecal PK, Pomraning E. CONVERGE Studio 3.0 2021.

[35] Richards KJ, Senecal PK, Pomraning E. CONVERGE 3.0 Manual, Convergent Science, Madison, Wisconsin; 2021.

[36] Richards KJ, Senecal PK, Pomraning E. CONVERGE Studio 3.0 Manual, Convergent Science, Madison, Wisconsin; 2022.

[37] Furze SF. Investigation of Fuel Efficiency in a Spark Ignition Opposed Piston Engine for Portable Power Applications. 3rd Year Undergraduate Engineering Project. University of East Anglia; 2018.

[38] Crankshaft for TD50Q, Chinese Motorcycle Parts Online (n.d.). https://www.chinesemotorcyclepartsonline.co.uk/part/CRS028 [accessed November 24, 2023].

[39] Autodesk Fusion360®; 2023.

[40] Internal Grooving, Sandvik Coromant (n.d.). https://www.sandvik.coromant.com/en-gb/knowledge/parting-and-grooving/internal-grooving [accessed November 24, 2023].

[41] Bosch Petrol Injector 026150001A (HDEV-5-1), OPIE OILS Website (n.d.). https://www.opieoils.co.uk/p-208263-bosch-petrol-injector-026150001a-hdev-5-1.aspx [accessed June 8, 2023].

[42] Sellnau M, Hoyer K, Petot JH, Kahraman E, Meissonnier G, Zermeno R, et al. Fuel injection system for opposed-piston gasoline compression-ignited (OP-GCI) engines. SAE Technical Papers 2019-April 2019. https://doi.org/10.4271/2019-01-0287.

[43] Venugopal R, Abani N, Mackenzie R. Effects of injection pattern design on piston thermal management in an opposed-piston two-stroke engine. SAE Technical Papers 2013;9. https://doi.org/10.4271/2013-01-2423.

[44] Roots blower (supercharger) by size, Ogura Clutch Co. Ltd (n.d.). https://www.oguraclutch.co.jp/product/ogura-super-charger-by-size/ [accessed January 24, 2023].

[45] Gates OE Type Coolant Thermostat (TH64978G1), OPIE OILS Website (n.d.). https://www.opieoils.co.uk/p-240628-gates-oe-type-coolant-thermostat-th64978g1.aspx [accessed April 21, 2023].

[46] Premixed Combustion Modelling, CONVERGE Training; 2020. https://hub.convergecfd.com/login [accessed June 7, 2023].

[47] Liu Y-D, Jia M, Xie M-Z, Pang B. Enhancement on a skeletal kinetic model for primary reference fuel oxidation by using a semidecoupling methodology. Energy Fuel 2012;26:7069–83. https://doi.org/10.1021/ef301242b.

[48] Blazek J. Computational fluid dynamics: principles and applications. Amsterdam: Elsevier Science; 2005.

[49] Jayanti S. In: Computational fluid dynamics for engineers and scientists. Dordrecht: Springer Netherlands; 2018. https://doi.org/10.1007/978-94-024-1217-8.

[50] Tu J, Yeoh G-H, Liu C. Computational fluid dynamics - a practical approach. 3rd ed. Elsevier; 2018. https://app.knovel.com/hotlink/toc/id:kpCFDAPA19/computational-fluid-dynamics/computational-fluid-dynamics.

[51] Atkins T, Escudier M. Favre averaging; 2013. 10.1093/acref/9780199587438.013.2107.

[52] Han Z, Reitz RD. Turbulence modeling of internal combustion engines using RNG κ-ε models. Combust Sci Technol 1995;106:267–95. https://doi.org/10.1080/00102209508907782.

[53] Fuel (VE) Table, Speeduino Manual; 2022. https://wiki.speeduino.com/en/configuration/VE_table [accessed May 19, 2023].

[54] Nave R. Alkanes, Hyperphysics (n.d.). http://hyperphysics.phy-astr.gsu.edu/hbase/Organic/alkane.html [accessed March 22, 2024].